nature reviews methods primers

https://doi.org/10.1038/s43586-023-00286-z

Primer

Check for updates

Brillouin microscopy

Irina Kabakova[1], Jitao Zhang[2], Yuchen Xiang[3], Silvia Caponi[4], Alberto Bilenca[5], Jochen Guck[6,7] & Giuliano Scarcelli[8,9]

Abstract

The field of Brillouin microscopy and imaging was established approximately 20 years ago, thanks to the development of non-scanning high-resolution optical spectrometers. Since then, the field has experienced rapid expansion, incorporating technologies from telecommunications, astrophotonics, multiplexed microscopy, quantum optics and machine learning. Consequently, these advancements have led to much-needed improvements in imaging speed, spectral resolution and sensitivity. The progress in Brillouin microscopy is driven by a strong demand for label-free and contact-free methods to characterize the mechanical properties of biomaterials at the cellular and subcellular scales. Understanding the local biomechanics of cells and tissues has become crucial in predicting cellular fate and tissue pathogenesis. This Primer aims to provide a comprehensive overview of the methods and applications of Brillouin microscopy. It includes key demonstrations of Brillouin microscopy and imaging that can serve as a reference for the existing research community and new adopters of this technology. The article concludes with an outlook, presenting the authors' vision for future developments in this vibrant field. The Primer also highlights specific examples where Brillouin microscopy can have a transformative impact on biology and biomedicine.

Sections

Introduction

Experimentation

Results

Applications

Reproducibility and data deposition

Limitations and optimizations

Outlook

[1]School of Mathematical and Physical Sciences, University of Technology Sydney, Sydney, New South Wales, Australia. [2]Department of Biomedical Engineering, Wayne State University, Detroit, MI, USA. [3]Department of Metabolism, Digestion & Reproduction, Imperial College London, London, UK. [4]Istituto Officina dei Materiali–National Research Council (IOM-CNR)–Research Unit in Perugia, c/o Department of Physics and Geology, University of Perugia, Perugia, Italy. [5]Biomedical Engineering Department, Ben-Gurion University of the Negev, Be'er-Sheva, Israel. [6]Max Planck Institute for the Science of Light, Erlangen, Germany. [7]Max-Planck-Zentrum für Physik und Medizin, Erlangen, Germany. [8]Fischell Department of Bioengineering, University of Maryland, College Park, MD, USA. [9]Maryland Biophysics Program, University of Maryland, College Park, MD, USA.
e-mail: irina.kabakova@uts.edu.au

Introduction

The effect of mechanical forces on tissue development and pathology was first recorded more than 100 years ago in relation to the structural formation of trabeculae bone[1]. At the smaller scale of a single cell, mechanical forces and changes in viscoelastic properties of intracellular and extracellular environments are as important to the cell function as biochemistry[2]. It took many decades, however, to acknowledge the role of mechanosensing and mechanotransduction in cell biology — the molecular mechanisms by which cells sense and respond to mechanical stimuli[3]. Largely, probing cells' mechanical properties with sufficient resolution and sensitivity, and without causing damage or changing their behaviour, is a very challenging task. The past 30 years have brought tremendous progress in experimental techniques for biomechanical measurements, and it is now agreed that mechanical forces play a crucial role in the development of many pathologies, including cardiovascular diseases and cancers[4,5].

Modern techniques for mechanical probing of cells and tissues include deformability cytometry[6], optical tweezers[7,8], atomic force microscopy (AFM) indentation[9,10], optical elastography[11], Brillouin microscopy[12–15] and other methods based on optical, mechanical and acoustic principles and their combinations (for example, picosecond ultrasonics[16] and time-domain opto-acoustic techniques[17,18]). Brillouin microscopy, the focus for this Primer, has the advantage of being a non-contact method capable of characterizing local micromechanical properties in biomaterials, compared with compression and rheology tests, traditionally used to measure volume-averaged elastic moduli (Fig. 1a). Brillouin microscopy relies on the principle of Brillouin light scattering (BLS), a process of inelastic scattering in which light interacts with gigahertz acoustic waves at the frequency Ω_B. Because of this interaction, the frequency of the scattered light undergoes a shift by exactly the acoustic frequency Ω_B (Fig. 1a). The detection of such frequency shift, called the Brillouin frequency shift (BFS), and its spectral line shape can lead to valuable insights into the local viscoelastic properties of biological samples[19]. As a label-free and contact-free method, Brillouin microscopy is suitable for in vivo and in situ 3D imaging of a broad range of biological systems[19–22].

In the spectral domain, a spontaneous BLS process in a homogeneous and isotropic medium produces Stokes and anti-Stokes peaks, located symmetrically around the elastically scattered Rayleigh band at frequency $f = 0$ as shown in Fig. 1b. Energy transfer from optical to acoustic waves produces downshifted Stokes light ($f = -\Omega_B$), whereas energy transfer from acoustic to optical waves produces upshifted anti-Stokes light ($f = +\Omega_B$). In most hydrated biological materials, including tissues and cells, BFS tends to be close to that of water, within the 5–8 GHz range. The absolute value of the BFS depends on the specific tissue, probing laser wavelength and scattering geometry. The linewidth of Brillouin peaks, Γ, falls between 100 MHz and a few gigahertz, and is also specific to the sample and the scattering geometry[13]. For a material with a known density and refractive index[23], Ω_B can be linked to the elastic response whereas Γ is linked to the viscous response of the material in the gigahertz frequency range, namely the longitudinal storage $M' \propto \Omega_B^2$ and loss $M'' \propto \Omega_B\Gamma$ moduli. Their ratio, the loss tangent, where $\tan\varphi = M''/M' = \Gamma/\Omega_B$, is a useful measure that neither depends on the refractive index nor density, and can be used to determine whether the mechanical properties alone influence the changes in M' and M'' over time[14,24,25].

Importantly, the longitudinal modulus probes the ratio of uniaxial stress to strain under a confined condition as opposed to the unconfined deformation used to define Young's modulus and shear modulus. As such, the longitudinal modulus corresponds to one of many components within the material elasticity tensor (the full tensor of an arbitrary material has a total of 81 components). The differences between the longitudinal, Young's and shear moduli are discussed in detail elsewhere[13,14]. BLS experiments are not restricted by measurements of the longitudinal modulus only but are capable of reconstruction of the full elastic tensor by varying the scattering angle as routinely performed for glassy and solid-state materials[26–28] and curing epoxy liquids[29]. Owing to a high level of hydration in biological matter, the frequencies of transverse and quasi-transverse phonons required for tensor reconstruction can fall below a few gigahertz and become particularly difficult to distinguish from the central Rayleigh peak[28]. Scanning the scattering angle at each measurement point adds additional time, making the full tensor reconstruction impractical for the current state-of-the-art Brillouin microscopy. Nonetheless, a few successful demonstrations of elastic tensor measurements in biological materials using BLS have been reported for collagen and silk fibres[25,30,31].

To resolve the shape of the Brillouin peak, an instrument resolution well below Γ is required. Pump–probe heterodyne techniques based on stimulated Brillouin scattering (SBS) achieve high spectral resolution <100 MHz, in theory only limited by the laser bandwidth[32,33]. Interferometric techniques using multi-pass Fabry–Perot spectrometers[34] or highly dispersive virtually imaged phase arrays, or virtually imaged phased arrays (VIPAs)[35], reach spectral resolution of 0.1–0.5 GHz.

Brillouin microscopy is sensitive to the local mechanical properties of materials. In heterogeneous samples, Brillouin spectra acquired at different points within the sample allow to build 2D and 3D images where Ω_B and Γ are used as contrast methods (Fig. 1c). The Brillouin images can depict the sample structures, help characterize tissue morphology[32,36,37], and visualize cell aggregates[38–41] and subcellular compartments[22,42–46]. These achievements make Brillouin microscopy a promising technique in many applications including biomedical diagnostics[47,48], mechanobiology[49–52], tissue engineering[53,54] and biomaterial characterization[55–57].

A peculiarity of Brillouin microscopy lies in the effective spatial resolution of the mechanical images. Unlike far-field optical microscopy, where the Abbe diffraction limit defines the reachable longitudinal and transversal spatial resolutions when the optical configuration is known, in Brillouin spectroscopy the light interacts with acoustic phonons that are extended collective excitations. Thus, both optical and acoustic fields need to be considered to define the spatial resolution of Brillouin images[58] (see Fig. 2 for an explanation of different spatial scales in Brillouin microscopy). The coherence length, l_c, estimates the characteristic size over which the density fluctuations probed by the BLS process are correlated. l_c is a sample-dependent parameter that can be estimated directly from the Brillouin spectra through the peak width, Γ, and position, Ω_B, knowing the phonon wavelength Λ, so that $l_c \sim \Lambda\Omega_B/\Gamma$ (ref. 59). l_c ranges from tens of microns in low dissipative solids to a few microns in high dissipative soft matter. When the coherence length is larger than the voxel of the focused optical beam, it represents the lowest reachable limit in the spatial resolution[60]. This limit influences the longitudinal as well as the transversal spatial resolution. In particular, the spatial extension of the phonons will be oriented with respect to the optical axis depending on the exchanged wave vector **q**. Hence, the angular distribution of the exchanged vector **q** influences the longitudinal and transversal spatial resolution: the use of high numerical aperture objectives can increase the longitudinal spatial resolution but can occur to the detriment of the transversal

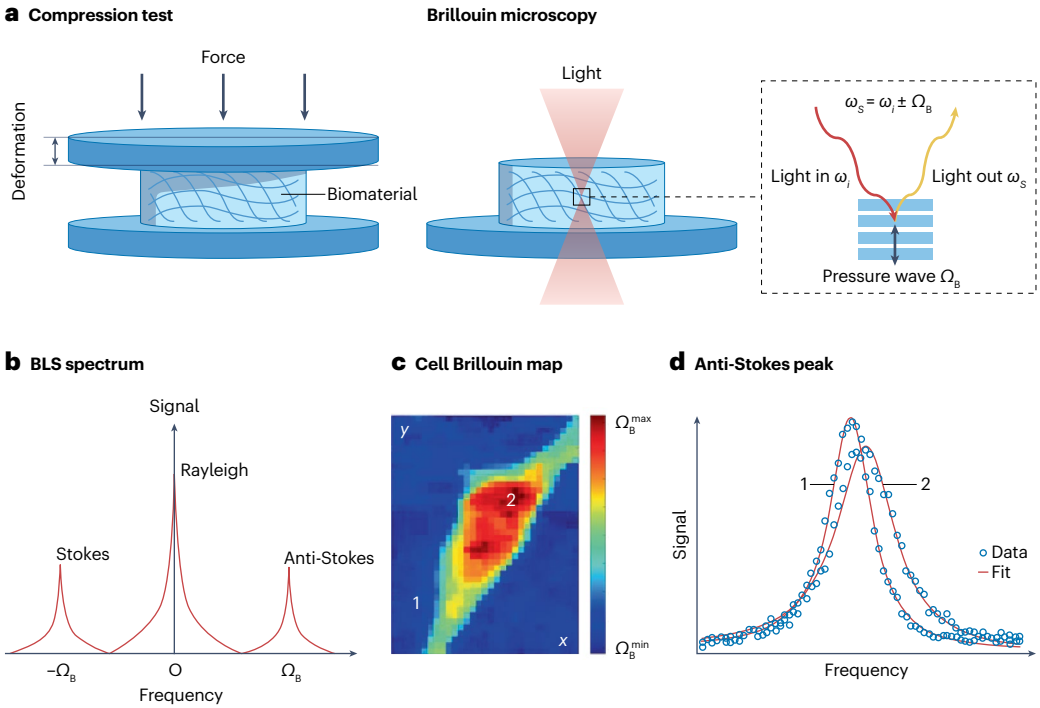

Fig. 1 | Principles of Brillouin light scattering microscopy. a, A conventional compression test (bulk properties) and Brillouin microscopy (local properties) for measuring mechanics in biomaterials. In Brillouin microscopy, a focused light beam is scattered by the gigahertz pressure waves producing ($\pm\Omega_B$) Brillouin frequency shift (BFS) of the scattered light. **b**, Brillouin spectrum showing a doublet of Stokes and anti-Stokes peaks, centred symmetrically around the unshifted Rayleigh scattered light. **c**, Brillouin map for a respiratory cell with colour coding indicating the BFS magnitude. **d**, Anti-Stokes peak for a location outside (1) and inside (2) the cell demonstrating the relative shift in Brillouin frequency across the sample. BLS, Brillouin light scattering.

one[60]. This intrinsic limit can be overcome in the specific case of phonon confinement, which occurs when the sample morphology contains structures characterized by significant acoustic mismatch with their environment and whose characteristic size is smaller than l_c. In this instance, BLS offers insights into the mechanical characteristics of nanostructures, for example in studies with nanoparticles[61,62] or thin films[59,63] where dimensions are comparable with the phonon wavelength (Λ ~300 nm).

The efficiency of the spontaneous BLS process depends on the material but is generally very low. For example, at room temperature the ratio between the number of inelastically scattered photons and the number of incoming photons is approximately one in a billion[64]. Additional losses within the optical system and collection optics mean that approximately 10^5 photons per second of 1 mW of incident visible laser power will be scattered and reach the detector[64]. The overall detected power typically is no larger than a nanowatt as each visible photon carries only 10^{-19} J of energy. Therefore, high quantum efficiency scientific-grade cameras and detectors should be used for Brillouin microscopy based on the spontaneous scattering process, preferably with electronic amplification such as electron-multiplying charge-coupled device cameras. Brillouin microscopy data typically have a low signal-to-noise ratio (SNR). One way to increase the SNR of the measurement is to collect the signal over a longer acquisition time. For confocal microscopy applications, however, this is too slow as many thousands of points within the sample need to be measured to complete the full sample scan. SBS methods can be one possible solution, as the efficiency of the stimulated scattering process is largely enhanced as compared with spontaneous scattering[32,33,65–67].

This Primer introduces the main methods of Brillouin microscopy and discusses the advantages, limitations and future directions in this vibrant field of research. Experimentation describes existing approaches to Brillouin microscopy, including spontaneous and SBS techniques, as well as practical aspects of the experimental set-ups including the requirements for the laser source, spectral filtering and biological sample preparation. The Results section showcases cell mechanobiology demonstrations and discusses Brillouin microscopy data processing approaches. Applications highlight the main areas of biomedicine and biology where Brillouin microscopy has already made significant impact or is expected to bring more advances in the future. The remaining sections address issues with reproducibility, data storage and deposition, challenges of Brillouin microscopy methods and the outlook for this field of research.

Experimentation

Depending on the nature of the biological sample and the intended application, various approaches to Brillouin microscopy can be adopted. The set-up for Brillouin microscopy can rely on either a single laser source, such as in spontaneous BLS, or multiple lasers, as seen in stimulated and impulsive Brillouin microscopy. In the following sections, the key considerations for assembling each type of Brillouin microscopy system are described, with a summary of the parameters presented in Table 1 and Fig. 3. Additionally, techniques for spectral

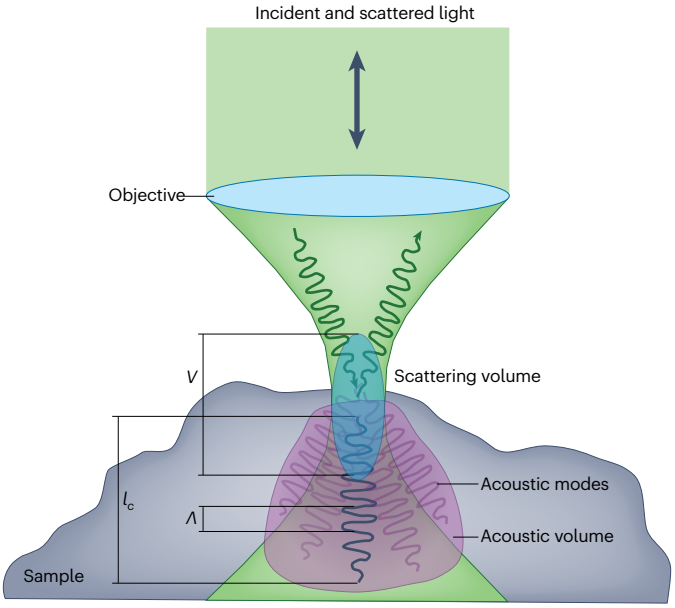

Fig. 2 | Length scales of the Brillouin light scattering process. The principal length scales that drive the spatial resolution of Brillouin spectroscopy. The scattering volume, V, which depends on the optical components (microscope objective and laser wavelength), the coherence length, l_c, which is a sample-dependent parameter that defines the so-called acoustic volume and, finally, the wavelength of the probed phonons, Λ. Adapted with permission from ref. 60 © The Optical Society.

filtering to eliminate unwanted light are described with comprehensive guidance for preparing biological samples, ranging from hydrogels to multicellular tissues and organoids.

Spontaneous Brillouin scattering techniques

Confocal microscopy. Brillouin spectroscopy has been traditionally performed with tandem Fabry–Perot (TFP) etalon scanning interferometry[68]. TFP-based Brillouin spectroscopy has represented the BLS experiment's workhorse for decades and still remains in widespread use for applied physics, material science[69] and environmental sensing[70]. Furthermore, in biomedical applications, TFP-based Brillouin spectroscopy has been reported for living cells[38], collagen fibres[30,71,72], hydrogels[53,54,57,73], the cornea and crystalline lens of the eye[74–76], biofilms[77,78] and bones[36,79,80]. Owing to the scanning operation modality, TFP spectrometers require long acquisition times. The fastest acquisition time reported using a TFP system to date requires 512 ms per single spectrum[78], with typical measurement speeds being tens of seconds depending on the transparency of the sample and imaging volume[36,57,73,81]. This characteristic makes it unsuitable for extensive characterization of a large area and/or large number of samples. Non-scanning Fabry–Perot spectrometers can shorten the acquisition time by removing the frequency scanning operation[79,82], but are limited in throughput as a significant portion of the light is lost in reflection. Introducing a VIPA, a different non-scanning etalon, fundamentally improves the Brillouin spectrometer speed (Fig. 4a). The back surface of a VIPA etalon is fully reflective, other than for a small input anti-reflection window, so that no light is lost in reflection resulting in increased throughput by approximately the etalon's finesse[35,82]. VIPA-based Brillouin confocal microscopy was first introduced in 2008 (ref. 12) and has been further optimized in the past 10 years to improve power throughput and noise rejection ability[83–88]. At present, the best Brillouin confocal microscopy systems exhibit an acquisition time ranging from 20 to 50 ms per pixel/spectrum within the shot-noise limited regime[20,42,52,89,90].

Line-scanning microscopy. Line-scanning Brillouin microscopy (LSBM) uses signal multiplexing, similar to light-sheet fluorescence microscopy[91,92]. In LSBM[93], one objective lens generates an illumination beam line, and the other collects the scattered light at 90° geometry for signal analysis of a multiplexed spectrometer (Fig. 4b), which enables simultaneous imaging and single-shot spectral analysis of hundreds of points with much lower irradiance dosage compared with confocal Brillouin microscopy. Therefore, the acquisition speed of the LSBM in biological samples can be more than one order of magnitude faster compared with confocal Brillouin microscopy, or up to 1 ms per pixel[37,39]. The multiplexing of the spectrometer is accomplished by aligning the illumination beam line perpendicular to the dispersion axis of a VIPA etalon. The lateral optical resolution of the LSBM is dictated by the numerical aperture of the collecting objective lens. The axial resolution is determined either by the size of the illumination beam or the collection objective's depth of field, whichever is the smallest. In practice, LSBM can be implemented in different forms. For instance, the illumination line can be generated by axially scanning the focus position with a tunable lens[37]; and a dual-line configuration has been developed to mitigate artefacts induced by the heterogeneous refractive index of a thick sample[39]. In addition, an epi-line geometry has been implemented for embryo samples[37].

Stimulated Brillouin scattering techniques

Stimulated Brillouin scattering microscopy. Stimulated Brillouin scattering (SBS) microscopy operates on the principle of stimulated light scattering, which occurs owing to induced variations in material density caused by optical waves. In SBS microscopy, two counter-propagating, continuous-wave, pump and probe laser beams (Fig. 4c), slightly detuned in frequency to match the BFS of the material Ω_B, are focused into a joint point in the sample to stimulate a longitudinal acoustic wave with frequency Ω_B. The acoustic wave, in turn, leads to a travelling grating of dielectric variations. Diffraction from this moving grating is detected as an increase (decrease), or gain (loss), in the probe intensity light at lower (higher) frequency. The gain magnitude is proportional to the pump power and influenced by material parameters such as mass density[66]. The SBS spectrum is acquired by scanning the pump–probe frequency detuning Ω over Ω_B (refs. 32,33,65,94–96). The notch filter is a rubidium gas cell used to suppress reflected stray light from the pump beam (Fig. 4c). An alternative approach to SBS microscopy that uses only a single pump laser and applies a heterodyne detection scheme has also been demonstrated[97].

To improve temporal resolution significantly, the SBS gain/loss can be recorded only at Ω_B. This is possible when preliminary knowledge of the sample properties is available, for example the range of BFSs[66]. Spectrum acquisition times down to 2 ms over 2 GHz in water and 20 ms over 4 GHz in living specimens are practical, resulting in adequate spectrum SNRs (~27–30 dB with overall incident power of ~230–265 mW). A larger frequency scanning range in biological samples may be required for a reliable multi-component fit analysis[32,98]. Spectral resolution similar to that in TFP-based Brillouin microscopy (~100 MHz) can be achieved in SBS microscopy and is determined by the laser linewidth, the frequency scanning-induced dispersion and

the aperture-induced spectral broadening[99]. SBS images are obtained by raster scanning the sample through the focus and measuring the SBS spectrum or the SBS gain/loss at Ω_B at each image pixel. The 3D spatial resolution of the SBS image is determined by diffraction and the non-linear excitation of SBS. For reduced incident power, SBS microscopy with squeezed light[100] or quasi-continuous-wave light has also been demonstrated[67,101]. Quasi-continuous-wave SBS, also known as pulsed SBS, is based on external modulation of the continuous-wave pump and probe by an acousto-optic modulator to form optical pulses of 10–100 ns. Depending on the pulse train duty cycle and the pump laser peak power, the overall radiation dose on the sample can be reduced by at least two orders of magnitude[67,101].

Impulsive stimulated Brillouin scattering microscopy. In impulsive stimulated Brillouin scattering (ISBS) microscopy, instead of using two continuous-wave laser beams, an optical pulse from a laser is divided into two pump beams focused into a joint point in the sample to produce a transient grating through the interaction between the pulsed light and the material (Fig. 4d). The generated acoustic wave is measured by the diffraction of a probe light that is incident to the focal point at the Bragg angle[102–108]. The probe light can be either continuous-wave or a delayed pulse depending on the time constants of the generated acoustic waves and the detection electronics[107,108]. Improved detection sensitivity is obtained by first mixing the diffracted light and the reference probe beam, and then measuring the intensity of the beat signal[106].

Requirements for the laser source

To achieve high-quality Brillouin microscopy measurements, the laser wavelength, power, spectral bandwidth and noise characteristics should be considered. The important laser characteristics for each type of Brillouin microscopy measurements are summarized in Table 1. Wavelengths within the biological transparency region (650–800 nm) are sought to be ideal to avoid sample photodamage[88]. Noteworthy, the efficiency of the scattering process declines rapidly with the light wavelength ($\sim\lambda^{-4}$), presenting a trade-off between the laser power and acquisition time. As with other optical microscopy methods, the penetration depth of Brillouin microscopy is limited by the sample absorption and multiple scattering and typically falls within the range of a few hundred microns.

Rayleigh band filtering

Brillouin signals are intrinsically weak and require additional filtering to be detected. Various strategies, passive or active, have been proposed for filtering unwanted light in the Brillouin system, which are generalized to the Rayleigh band as they are difficult to distinguish spectrally. Passive filters, commonly used in other spectroscopy methods for their simplicity and stability, are challenging to implement for Brillouin microscopy, owing to the requirement of a narrow notch/edge width (<10 GHz). Thin film technology is limited to around 100 GHz in width and cannot be achieved passively[109]. To overcome this, atomic/molecular filters based on gas absorption bands can be used, providing an additional 50 dB of extinction. However, the availability of these filters depends on the materials used, although popular bands such as 780 nm can be targeted[110]. It is important to note that some absorption agents may cause residual absorption of Brillouin signals, leading to spectral asymmetry and negatively affecting data interpretation. An alternative passive filtering design, based on spatial frequency filtering by using a Lyot stop[87], is simple and readily available, but has a limited 20 dB extinction.

Active optical filtering strategies have also been successful in providing extra spectral contrast for Brillouin microscopy. A common-path interferometric notch filter is another approach that can help reach 50 dB extinction[111]. The device's long-term stability is achieved by using feedback closed-loop control and adjusting the glass positioning adaptively. To suppress amplified spontaneous emission, Bragg gratings and Fabry–Perot etalons can be combined, achieving ~90 dB of amplified spontaneous emission suppression[37,39]. Spatial separation of unwanted light using multiple dispersive elements and filter masks is another well-established approach, such as introducing another

Table 1 | Requirements for the laser source

Technique	Laser type	Output power/energy	Spectral characterization
Spontaneous Brillouin microscopy[12,20–23,28,38,40,41]	Single longitudinal mode laser	>50 mW	Linewidth: <10 MHz Spectral purity: >60 dB Frequency stability: <0.2 GHz h^{-1}
Continuous-wave SBS[32,33,65]	Tunable continuous-wave lasers	Pump: >180 mW Probe: >40 mW	Tuning range: >2 GHz Linewidth: <10 MHz Preferably locked to a frequency standard
Pulsed SBS[67,101]	Tunable continuous-wave lasers with an additional electro-optic or acousto-optic modulator to form pulses	Pulse duration: 10–100 ns Repetition rate: 0.5–1 MHz Peak power: 0.1–1 W (pump) 10–100 mW (probe)	Tuning range: > 2 GHz Linewidth: <10 MHz Preferably locked to a frequency standard
Impulsive SBS[102,104,105]	Pulsed laser (pump)	Pulse energy: >10 μJ Pulse duration: ~1–10 ps	Energy stability: <2% rms
	Continuous-wave laser (probe)	Power: >40 mW	Single frequency operation Linewidth: <10 MHz

SBS, stimulated Brillouin scattering.

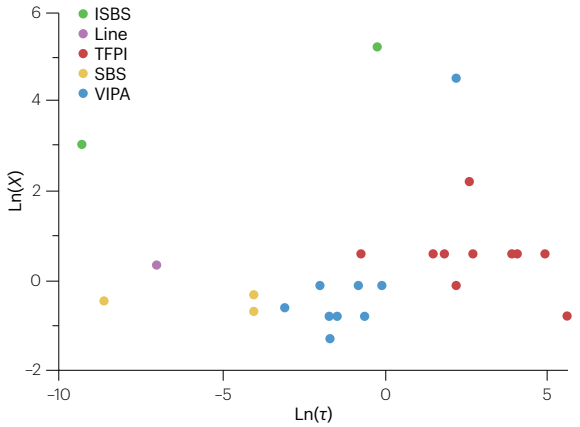

Fig. 3 | Characteristic parameters of Brillouin microscopy experiments. The acquisition time per pixel, τ (seconds) and the lateral imaging resolution, X (microns). Parameters are based on the following experiment type: tandem Fabry–Perot interferometer (TFPI)[36,38,53,54,57,76,78,139,155,187], virtually imaged phase array (VIPA) spectrometer[12,19,20,22,24,41,42,52,150,165], line-scanning VIPA spectrometer (Line)[37,39], stimulated Brillouin scattering (SBS) microscopy[32,67,100] and impulsive stimulated Brillouin scattering (ISBS) microscopy[102,103]. Further details on the sample type are presented in Supplementary Table 1.

VIPA in the spectrometer placed orthogonal to the first, resulting in an extra 30 dB of extinction with a well-designed mask[112]. Similar blocking effects can be achieved in the Fourier domain[44].

The active strategy used in TFP set-ups employs the multi-pass configuration: the light passes three times through each of the two Fabry–Perot interferometers, which synchronously perform a scan. The movement of the mirrors and their alignment are actively controlled in real time by piezoelectric transducers. Such a spectrometer is characterized by high resolution and high contrast: the newly developed configuration, TFP-2 HC, reports the record-high contrast of 150 dB (ref. 78). With the emergence of high-throughput LSBM configurations[37,39], it may become necessary to combine various passive and active filters. Therefore, a balanced trade-off between optical throughput and overall extinction ratio should be considered during experimental design.

Sample preparation and considerations

Hydrogels. Hydrogels are commonly used for designing 3D cell and tissue models as they mimic the natural extracellular matrix and provide cells with mechanical support, hydration and delivery of nutrients. Owing to relative simplicity and ability to control the gel fabrication process, this biological material presents a viable model for Brillouin microscopy benchmarking and standardization[15]. For example, efficient tuning of mechanical properties (Fig. 5a) was demonstrated in gelatin hydrogels[53,113]. Additionally, hydrogel beads can be used for characterization of the sample heterogeneity[114–116]. Important aspects to consider in the preparation of hydrogel models for Brillouin microscopy imaging are time-dependent swelling and non-uniform gel hydration[117]. The incubation of hydrogels in media can cause the gel's polymer network to swell and a dynamic increase of the local hydration in the 48 h post incubation. Furthermore, cross-linking of gels and tissues results in material stiffening and reduction in local hydration. The effect of hydration on the BFS and linewidth has been investigated in various fibrous materials[30], gelatin gels[118], hydrogels[117,119,120] and human corneas[121,122]. The impact of hydration changes on the longitudinal modulus and BFS has been elucidated using a two-phase model[117,121]. It was found that the dehydration process occurring in collagen gels displays the same behaviour as in the glass transition process, for example the phase transition process in amorphous materials from a liquid-like to a solid-like glassy state. In this case, the polymer concentration is the control parameter and plays the same role as temperature or pressure in the analytical description of the transition[53] (Fig. 5a). It is crucial to exercise caution while devising Brillouin imaging experiments to maintain a consistent hydration level. One feasible approach is to permit samples to gradually swell over time until they attain a state of equilibrium hydration.

Single cell. A single cell typically has a size ranging from a few micrometres to several tens of micrometres, and its mechanical properties are sensitive to changes in the surrounding microenvironment (Fig. 5b). When probing cellular biomechanics using Brillouin microscopy, it is essential to maintain cells in their physiological or culture conditions. A good practice is to keep cells within an on-stage incubation chamber that ensures a suitable environment such as the temperature, humidity, and CO_2 and O_2 levels. For Brillouin microscopy with an inverted configuration, whenever feasible, the substrate for cell attachment should be thin and optically clear to minimize beam distortion. If appropriate, cells can be seeded on a Petri dish with a glass coverslip bottom (thickness <200 μm).

Owing to the strong back-reflection from the interface of the glass bottom and cell culture medium, noise from non-scattered light can become significant when the focal plane is close to this interface. In such cases, additional background filtering and noise reduction techniques may be necessary to extract the Brillouin signal[44,86]. Alternatively, the bottom of the dish can be pre-coated by a thin hydrogel layer (<500 μm) to match the refractive index of the medium, thus reducing back-reflection[42]. However, as cells may adjust their mechanical properties in response to a substrate's stiffness[22], the impact of the hydrogel layer should be carefully evaluated based on the purpose of the experiment. In addition, many standard culture media contain phenol red, which is a pH indicator but can photosensitize cells with strong absorption of visible light. To reduce the risk of phototoxicity, it is recommended to replace the standard medium with a phenol red-free alternative before conducting Brillouin microscopy experiments[88].

Tissues, spheroids and whole organisms. Compared with single cells, multicellular samples such as biological tissues, spheroids (Fig. 5c) and whole organisms have larger size, more heterogeneous distribution of biomechanics and more complicated compositions. Therefore, careful consideration should be given to the trade-off between spatial resolution and acquisition time, sample preparation and orientation and data interpretation. For time-extended experiments, the potential phototoxicity should be carefully considered. Brillouin microscopy has been used for quantifying a broad range of biological tissues ranging in size from ~100 μm to a few millimetres, including ocular tissues (for example, cornea, retina and crystalline lens)[76,123–129], central nervous system tissues (such as cortex, putamen, corpus callosum, hippocampus and spinal cord)[52,130], muscle, skin, cartilage and early-stage embryonic tissue[20,89,131] (Fig. 5d–f). The acquisition speed of the Brillouin microscope can be altered, for example 20–500 ms per pixel, to preserve the biomechanics of the sample throughout the acquisition time and to allow sufficient mechanical details to be captured. However, the size of the mapping area and spatial resolution may become compromised.

Ocular tissue, such as the cornea, is among the outmost layer of an eyeball and possesses excellent optical transparency, allowing for in vivo testing[121,132]. Notably, zebrafish, especially in the larval stages, are relatively transparent and can be investigated completely in vivo[20,52,127–129]. Otherwise, biological tissues generally need to be prepared to fit a standard Petri dish or glass slide for ex vivo testing. To avoid alteration of tissue biomechanics, live tissue without fixation or freezing is required, even though the sacrificing of animals and the cutting required can lead to changes in material properties[52]. Considering the penetration depth of Brillouin microscopy of a few hundred microns[133], the region of interest should be as close to the surface as possible. For anisotropic tissue such as the cornea, the orientation of the tissue layer should also be specified[134,135]. Additionally, Brillouin data can be carefully calibrated against conventional methods such as AFM[22].

3D cell culture such as spheroids represents a physiologically more relevant culture system compared with conventional 2D cell culture[136]. With its ability to provide subcellular resolution in three dimensions without physical contact, Brillouin microscopy is well suited for mapping biomechanics of spheroids (Fig. 5c). In experiments, spheroids can be prepared in different ways: embedding cells into hydrogel, placing cells into a low attachment well or seeding cells on top of soft Matrigel[19,38,40,137,138]. In confocal Brillouin microscopy, experiments can be conducted in the spheroids' native culture. Alternatively, LSBM can be used for rapid mapping with a lower irradiation dose[39]. Here, spheroids must be harvested and embedded in an agarose gel, although this can be overcome when using an inverted microscope[37]. Brillouin technology can also be used for whole organisms, such as *Caenorhabditis elegans*[32] (Fig. 4e). To acquire biomechanical maps of live *C. elegans* using stimulated Brillouin microscopy, the sample along with growth medium is transferred to a homemade mount that sandwiches the sample between two coverslips. Two counter-propagating laser beams, namely the pump and the probe, pass through the coverslips and intersect at the common focal plane within the sample, allowing for the acquisition of Brillouin images through the raster scanning of the sample.

Results

Data acquisition and processing

Brillouin line shape analysis in homogeneous and heterogeneous materials. The mechanical and thermodynamic properties of materials determine the spectral features of Brillouin signals. In a bio-Brillouin framework, the analysis considers the position of Ω_B and the full width at half maximum Γ of the Brillouin peak associated with the longitudinal acoustic wave. Close to Ω_B, the spectrum can be described by a damped harmonic oscillator convoluted with the experimental response function $R(\Omega)$:

$$I(\Omega) = \frac{I_0}{\pi} \frac{\Omega_B^2 \Gamma}{(\Omega^2 - \Omega_B^2)^2 + \Omega^2 \Gamma^2} \otimes R(\Omega) \quad (1)$$

where I_0 is the peak intensity and $R(\Omega)$ considers the peak enlargement, owing to the finite spectrometer resolution, and the spread in the exchanged phonon wave vectors, owing to the aperture of the focusing and collection optics[36,139]. In low dissipation conditions, such as $\Gamma \ll \Omega_B$, the damped harmonic oscillator function can be approximated by a Lorentzian peak.

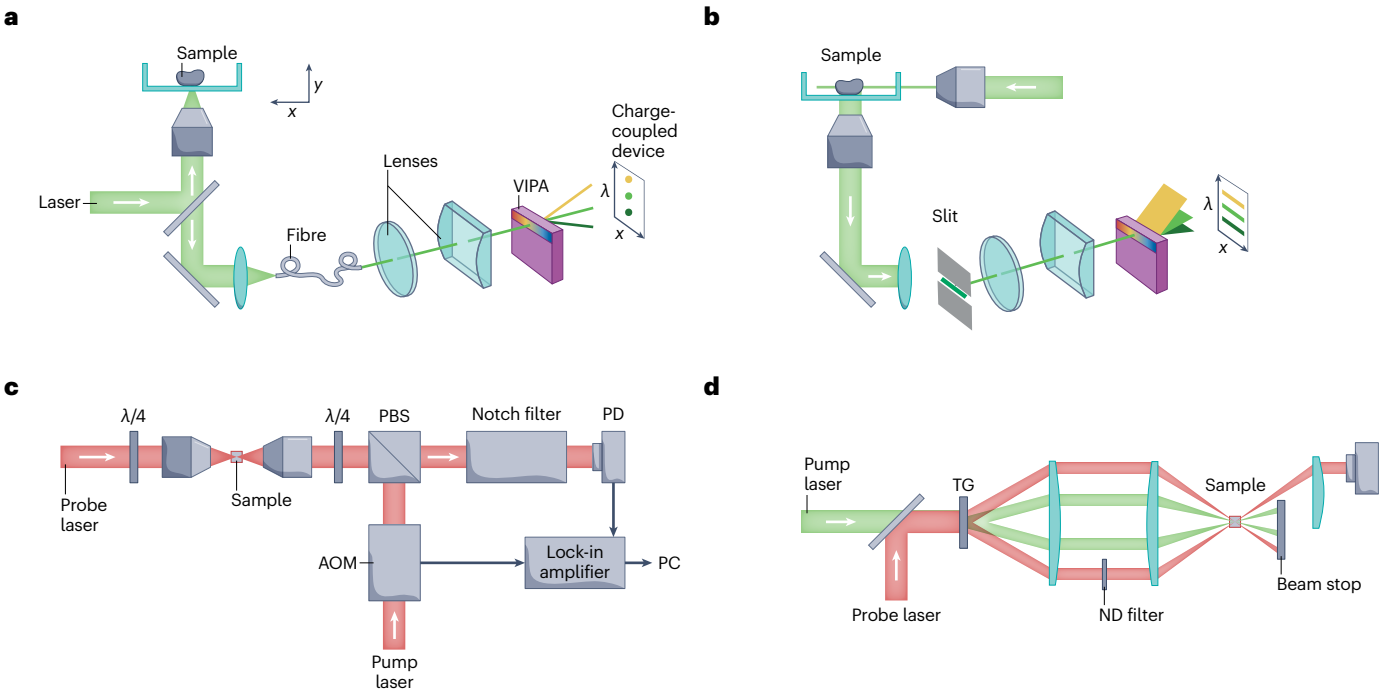

Fig. 4 | Brillouin imaging technology. a, Confocal Brillouin microscopy. **b**, Line-scanning Brillouin microscopy (LSBM). **c**, Continuous-wave stimulated Brillouin scattering (SBS) microscopy. **d**, Impulsive stimulated Brillouin scattering (ISBS) microscopy with heterodyne configuration. $\lambda/4$, quarter-wave plate; AOM, acousto-optic modulator; ND filter, neutral density filter; PBS, polarized beam splitter; PC, personal computer; PD, photodetector; TG, transmission grating; VIPA, virtually imaged phased array.

For elastically heterogeneous samples, the final spatial resolution and the Brillouin peak line shape are derived from the spatial extension of the probed acoustic waves[60]. Depending on the characteristic size of the heterogeneities, l, and on the acoustic mismatch among them, two scenarios are possible[59]. If the scattering volume is filled by heterogeneities characterized by $l < l_c$ (where l_c is the phonon coherence length) with a small acoustic mismatch, a single phonon can extend across different structures and a single broadened Brillouin peak is expected in the spectrum. In this case, Γ accounts for all of the different phonon attenuation processes and Ω_B provides an average

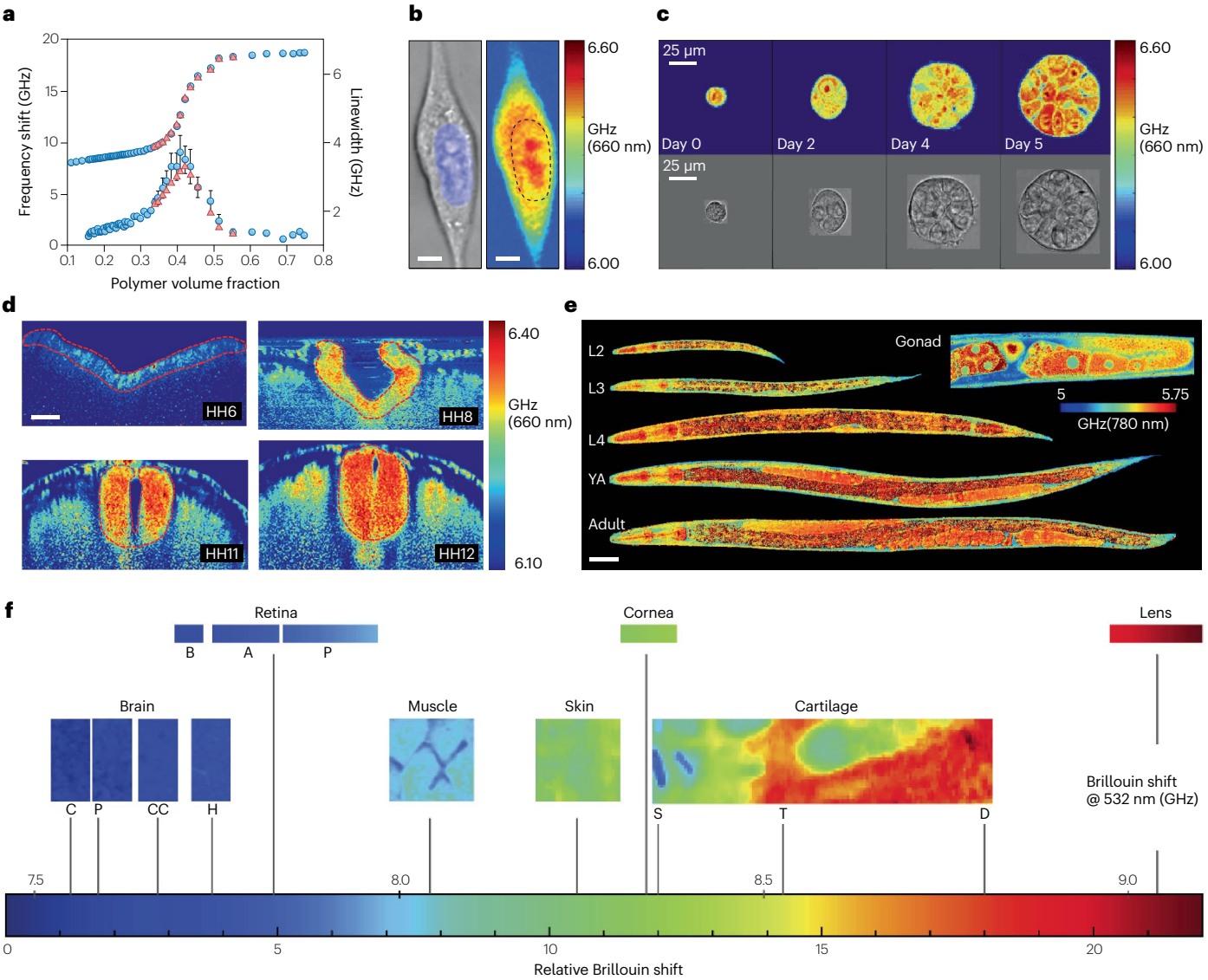

Fig. 5 | Representative data obtained using Brillouin technology. a, Brillouin frequency shift (BFS) and linewidth of gelatine versus polymer volume fraction, acquired by a spontaneous Brillouin microscope with 532 nm laser source. Red triangles represent theoretical values derived from the viscoelastic fit. **b**, Brillouin image of a live 3T3 cell, acquired by a spontaneous Brillouin microscope with 660 nm laser source. Blue shadow and dashed line indicate the cellular nucleus. Scale bar: 5 µm. **c**, Brillouin images of a single cell and three spheroids at different stages of growth, acquired by a spontaneous Brillouin microscope with 660 nm laser source. The human breast cancer line MCF10CA1h was used. Scale bar: 25 µm. **d**, Brillouin images of cranial neural tube tissue of four embryos at different culturing stages, acquired by a spontaneous Brillouin microscope with 660 nm laser source. Red dashed line outlines the neural plate region. Scale bar: 50 µm. **e**, Brillouin images of live nematodes at three larval stages (L2–L4) and two adult stages, acquired by a stimulated Brillouin microscope with 780 nm laser sources. Scale bar: 50 µm. Insert is a magnified image of the gonad. Scale bar: 25 µm. **f**, BFS values for various tissues, acquired by a spontaneous Brillouin microscope with 532 nm laser source: brain tissue (cortex (C), putamen (P), corpus callosum (CC), hippocampus (H)), cartilage tissue (superficial (S), transitional (T), deep (D)) and retina tissue (basal (B) – nerve fibre layer, retinal ganglion cell layer, inner plexiform layer; apical (A) – inner nuclear layer, outer plexiform layer; and photoreceptor cell layer (P) – outer nuclear layer, photoreceptor inner segment, photoreceptor outer segment). HH, Hamburger Hamilton staging; YA, young adult. Part **a** reprinted from ref. 53, CC BY 4.0. Part **b** reprinted from ref. 133, Springer Nature Limited. Part **c** reprinted with permission from ref. 137, Elsevier. Part **d** adapted from ref. 201, Springer Nature Limited. Part **e** adapted from ref. 32, Springer Nature Limited. Part **f** adapted with permission from ref. 130 © The Optical Society.

value of the sample mechanics. On the contrary, when $l > l_c$ or the acoustic mismatch is very high, the phonons are confined within the heterogeneities allowing to determine their mechanical properties. This latter condition was recently found in a study investigating human bones[36,80].

Effect of the variation of refractive index and density on frequency shift. The BLS measurement output is the frequency shift, Ω_B, which – in addition to the longitudinal storage modulus M' – also depends on the refractive index, n, and the mass density, ρ, at the measurement location within the sample:

$$\Omega_B = \frac{2n\sin(\theta/2)}{\lambda}\sqrt{\frac{M'}{\rho}} \quad (2)$$

where θ is the scattering angle and λ is the laser wavelength. Both n and ρ typically scale with local electron density so that the ratio between them is at least constant, or even trivially cancels. For this reason, these two parameters are often not considered, and the BFS is interpreted as a direct proxy of the longitudinal modulus. Further, in some cases the variability of the refractive index across a tissue being measured, such as for zebrafish spinal cord, has directly been quantified using quantitative phase imaging and found to be much smaller than the variability of the BFS[52].

However, there are instances where the ratio between n and ρ changes within a biological sample, which could lead to misinterpretation of the BFS data. The contribution of some of the most abundant biomolecules found in biological cells, such as proteins, nucleic acids and phospholipids, to the refractive index and density can be considered using a two-substance mixture model[140]. For each material, there is a so-called refraction increment that can vary by almost a factor of two between proteins and phospholipids, for example. As certain areas within cells have different compositions of these biomolecules, it is necessary to measure both the local refractive index and the mass density explicitly for accurate conversion from BFS to the longitudinal modulus. This is particularly obvious for lipid droplets within adipocytes, which have higher refractive index but lower mass density than water and where the two-substance mixture model cannot be applied, as it can translate to an error of up to 20%[46]. The 3D refractive index distributions within a cell can be determined by optical diffraction tomography with spatial resolutions of about 100 nm (ref. 141). Mass density can be extracted from the gain in stimulated Brillouin spectroscopy[66] or computed from the known refractive index – if the assumptions of the two-substance mixture model are fulfilled and if the local composition of biomolecules is known. The local chemical composition can be either estimated from fluorescence microscopy[46] or, even better, Raman spectroscopy[78], ideally all in one instrument.

Line broadening and asymmetry of the Brillouin peak. The asymmetric line shape of the Brillouin peak, accounted for by the damped harmonic oscillator fitting function, derives from the intrinsic attenuation processes present in the material and is particularly evident when investigating highly dissipative samples[142]. There are additional effects that distort and broaden Brillouin peaks, which require further discussion (Fig. 6).

The linear dispersion relation $\Omega_B = v\mathbf{q}/2\pi$ links the BFS, Ω_B, to the exchanged wave vector $\mathbf{q} = 2\pi n/\lambda \sin(\theta/2)$, with v being the sound velocity of the acoustic modes (see Eq. (2)). This implies that each $\mathbf{q}$ corresponds to a specific Ω_B. The use of high numerical aperture (NA) focusing and collecting optics introduces a large distribution of possible scattering angles θ, extending the range of the exchanged wave vectors[60,143]. The resulting spectral distortions depend on the chosen microscope objective and the scattering geometry used.

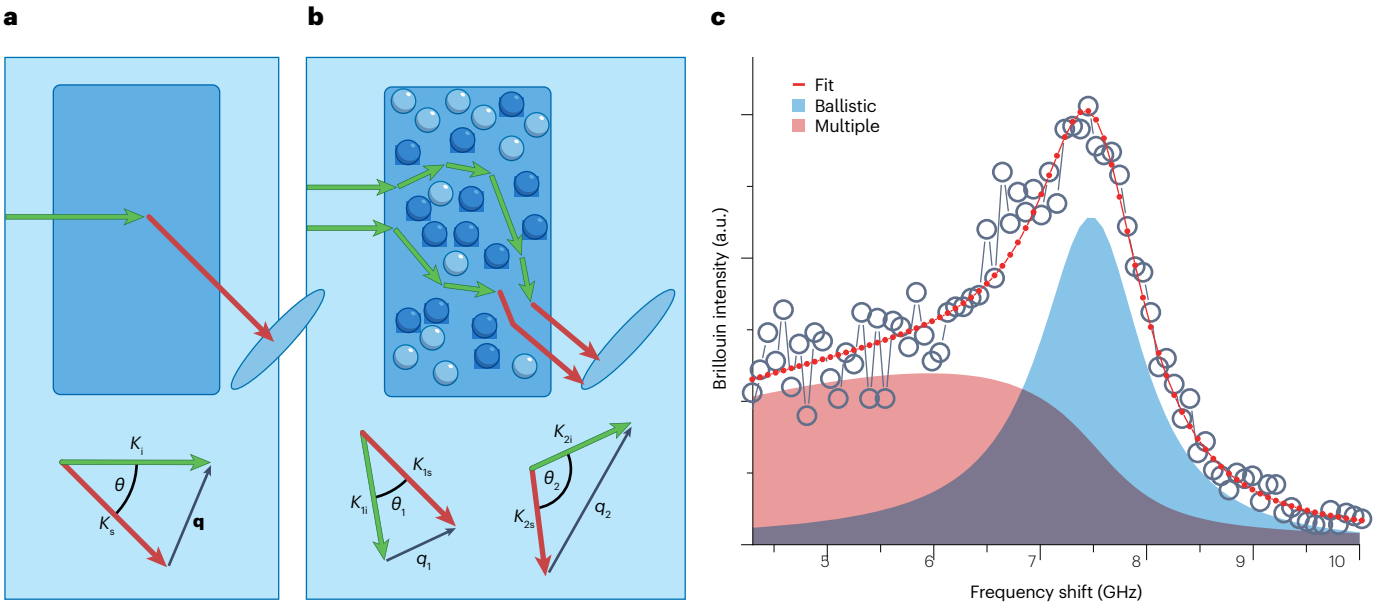

Fig. 6 | Ballistic and multiple Brillouin scattering processes. a, A Brillouin light scattering (BLS) process occurring in a transparent medium, where all scattered photons are ballistic and the scattering geometry defines the exchanged vector $\mathbf{q}$. **b**, A multiple scattering process introduces uncertainty in the $\mathbf{q}$ value. **c**, Brillouin spectrum (markers) acquired in the depth of a milk sample: ballistic (solid blue line) and multiple scattering (dot–dash line) contributions are provided. θ, scattering angle; K_i, wave vector of incoming light; K_s, wave vector of scattered light. Adapted from ref. 144, CC BY 4.0.

In back-scattering, where the exchanged wave vector reaches its maximum, high NA optics implies a reduction in the effective **q**, corresponding to the introduction of a low-frequency tail in the peak, which modifies its frequency position and width[99,139,143]. Here, effective NA is important rather than nominal NA of the microscope objective lens, as the objective aperture can become underfilled, resulting in NA reduction.

The linewidth distortions are even more important when investigating turbid media. In fact, the propagation direction of light inside turbid systems continuously changes so that the external scattering geometry no longer defines the effective scattering angle θ. Recently, polarization gated Brillouin spectroscopy has been introduced to selectively determine the contributions in the Brillouin spectra, owing to the ballistic and the diffusive photons[144] (see Fig. 6a,b). Both the use of high NA objectives and the influence of multiple scattering effects can be individually quantified or simulated (Fig. 6c), allowing for the spectra to be effectively analysed in a suitable manner.

Data pre-processing. Brillouin microscopy data analysis is non-trivial owing to its high dimensionality. Prior to analysis, pre-processing steps are necessary to enhance data quality and interpretability. Although widely available for biomedical spectroscopy[145], there is currently no standardized approach for Brillouin microscopy. In data sets acquired using low-contrast spectrometers, subtracting the Rayleigh band prior to analysis is essential, as it can directly affect the accuracy of the extracted information. Software filtering, such as direct subtraction using a pseudo-Voigt function[146], is possible in addition to hardware filtering. Data normalization and scaling are additional pre-processing steps that remove systematic variabilities, allowing for the identification of subtle biological patterns. For example, methods such as standard normal variate transformation have been effective in stabilizing variance for subsequent analyses[146]. Brillouin microscopy data typically have low SNRs; denoising techniques such as wavelet and maximum entropy reconstruction have thus been proposed[147], providing useful spectral signals even from challenging photon statistics (SNR ≥ 1). More recently, the matrix pencil method has shown promise for denoising non-linear Brillouin signals in the temporal domain[148]. Enhancing the SNR post acquisition may allow for faster imaging speed by sacrificing some photon budget experimentally and restoring it computationally.

Univariate analysis and peak detection. Although Brillouin microscopy data are intrinsically high-dimensional, they are often sparse in the spectral domain. To analyse the data, peak fitting methods are commonly used to compute the peak position and width, which relate to bulk compressibility and viscosity, respectively. Different profiles such as the Lorentzian function, pseudo-Voigt function and damped harmonic oscillator have been employed to handle various assumptions and experimental set-ups[15,146]. Directly analogous to the same concept in localization microscopy, successful peak fitting allows super-resolution in spectral localization but is still fundamentally limited by detection and noise models, bound by information theoretic limits. This precision limit has been derived for different experimental parameters[149] and should facilitate the performance evaluation of various hardware and software aspects of Brillouin microscopy, such as denoising tools. Interestingly, determining the spectral linewidth is more challenging and less accurate. Once average peak locations and widths are obtained for each spatial location in the Brillouin microscopy data, mechanical contrast images are formed. Univariate statistics can then be applied for hypothesis testing between different regions of interest or samples. For instance, *t* tests and analysis of variance with Bonferroni false discovery correction have been used to evaluate differences in Brillouin peak properties from various samples such as 3D bioprinted hydrogels, dentin and mice arterial sections[56,57,150]. Fitting, usually by means of least-square algorithms, can however become time consuming, especially for larger Brillouin microscopy data sets consisting of $>10^4$ pixels. As such, other approaches such as use of the spectral phasor and moment have also been presented[151,152]. The spectral phasor is a fitting-free method, widely used in other complex imaging data owing to excellent noise resilience. On the other hand, the moment approach is routinely applied for Raman data and can separate overlapped peaks assuming spectral symmetry. Both methods utilize faster computational processes, providing quicker options for data visualization.

Unsupervised and supervised multivariate analysis. Considering the subtle spectral variations, it is often advantageous in Brillouin microscopy to analyse the entire spectral domain using multivariate analysis. Multivariate analysis explores the correlations between different spectral variables across the data set (Fig. 7). This approach, widely used in hyperspectral imaging, for example in remote sensing, leverages machine learning capabilities. Multivariate algorithms can be supervised or unsupervised depending on the level of prior knowledge required (Fig. 7). Although various algorithms are applicable to Brillouin microscopy with minimal modification, representative algorithms for high-level image analysis applications are discussed, without delving into their inner workings (more details can be found elsewhere[146]). Unsupervised analysis finds patterns in input data without any prior knowledge. Principal component analysis (PCA) performs a linear transformation of the input data into a set of basis vectors that are defined by the ranked intra-data variances, in turn projecting Brillouin microscopy data into distinct spectral components. This form of dimension reduction is one of the enabling powers of multivariate analysis, as it provides easy 2D/3D visualization and exploration of data trends, even in large, complex high-dimensional data. One important confounding factor in analysis of Brillouin microscopy data is that a spectral mixture can be acquired from a single spatial location. Spectral unmixing using methods such as minimum volume simplex analysis and non-negative matrix factorization have been proposed to separate overlapped components, also known as endmembers[153,154]. The number of endmembers dictates the algorithm performance, which can be estimated statistically or manually. The former can be realized by observing the natural groupings in the data and is directly linked to the idea of cluster analysis. *K*-means cluster analysis and other fast density-based clustering methods are efficient for stratifying high-resolution Brillouin microscopy data[146,155]. Similarly, clustering can also be performed more optimally in a dimensionally reduced latent space by combining with, for example, PCA.

Supervised analysis, on the other hand, requires prior knowledge for optimal functioning. It is useful for spectral classification and hypothesis testing, for example distinguishing diseased versus healthy samples. Although still rarely practised, the supervised classification of Brillouin microscopy data was first demonstrated on fat cells using linear discriminant analysis (LDA)[146] and more recently adapted to discover spectral markers for the diagnosis of osteoarthritis[36]. On the back of successful implementations in related fields, the use of supervised deep learning is also anticipated to impact future Brillouin microscopy data analysis, especially in terms of multimodal integration and developing machined

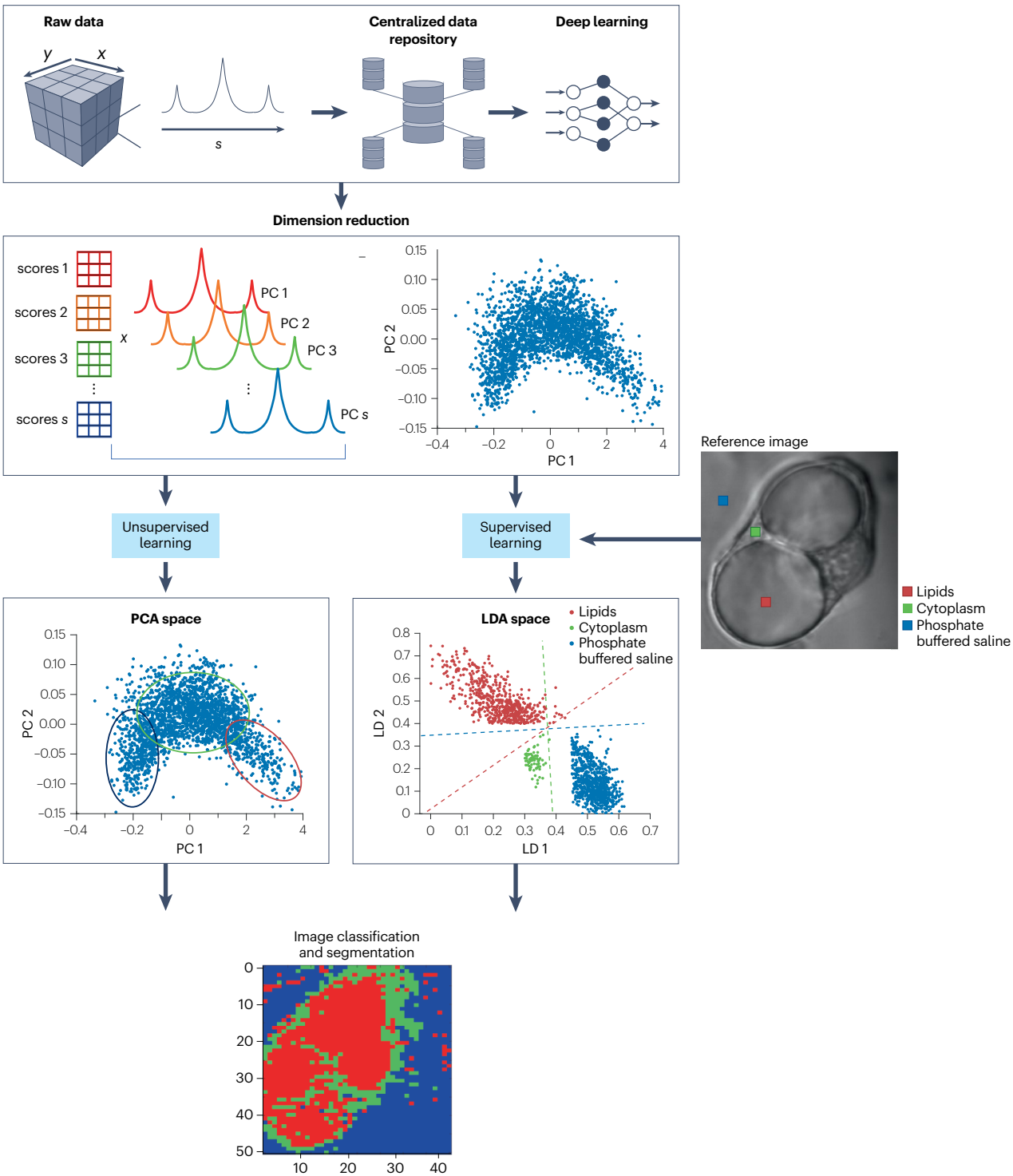

Fig. 7 | A typical workflow depicting analysis of Brillouin microscopy data with modern machine learning approaches. The high-dimensional raw data can generally be more easily interpreted through dimension reduction, for example by principal component analysis (PCA) as illustrated. The lower-dimensional representation can be used with unsupervised learning techniques, where natural trends and patterns in the data can be extracted statistically to divide the data into clusters and visualized spatially (segmentation); alternatively, supervised learning approaches may also be used with additional prior information, for instance labels of distinct cellular regions from another reference image. A model can then be trained using these labels with, for example, linear discriminant analysis (LDA), where the best-performing model can then be used to predict the class of unseen pixels or images (classification). With the increase in data quality and quantity, a centralized repository hosting a wide range of Brillouin microscopy data from different detectors, sources and domains can also be envisioned to enable deep learning approaches in the near future. Adapted with permission from ref. 146, Wiley.

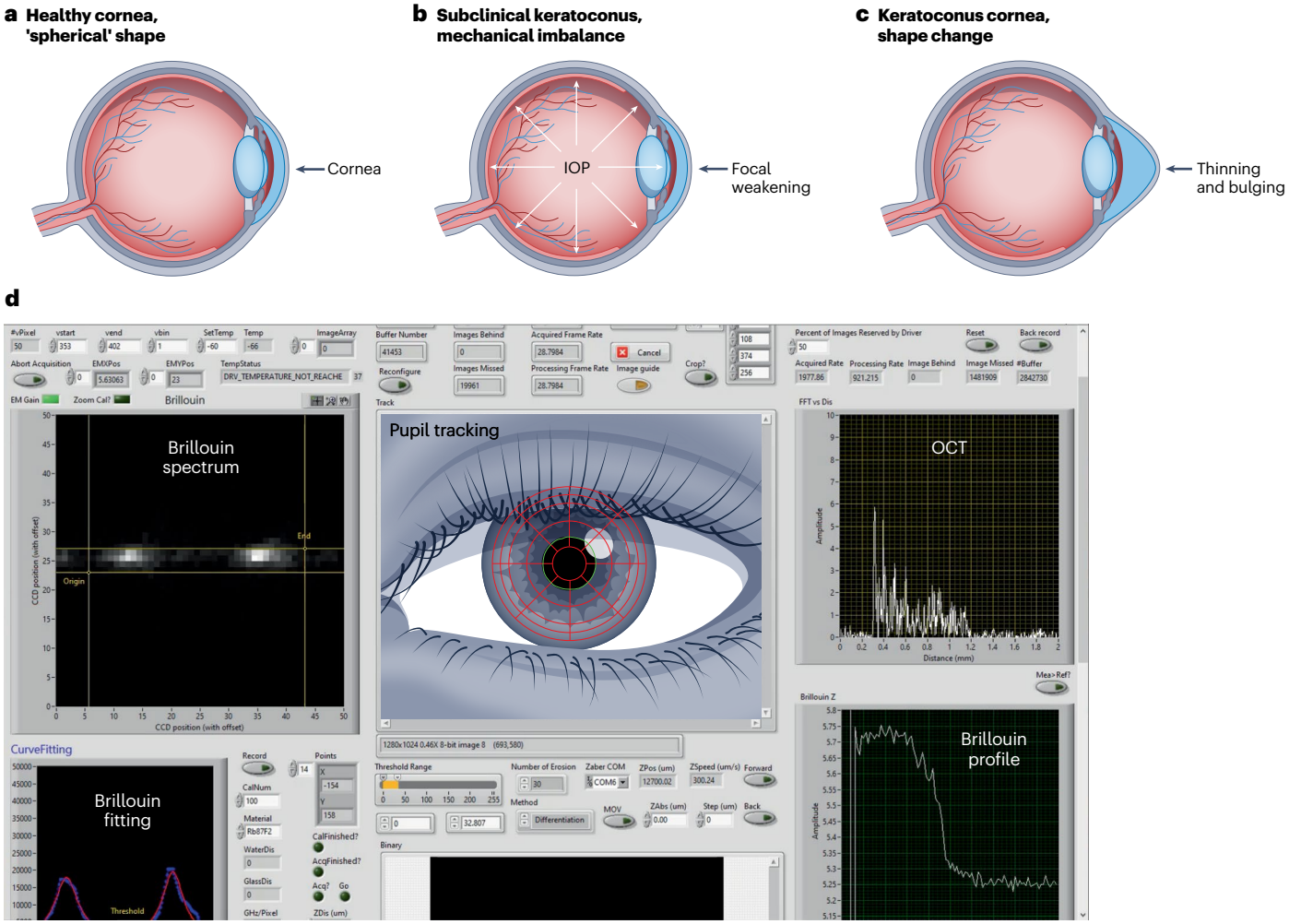

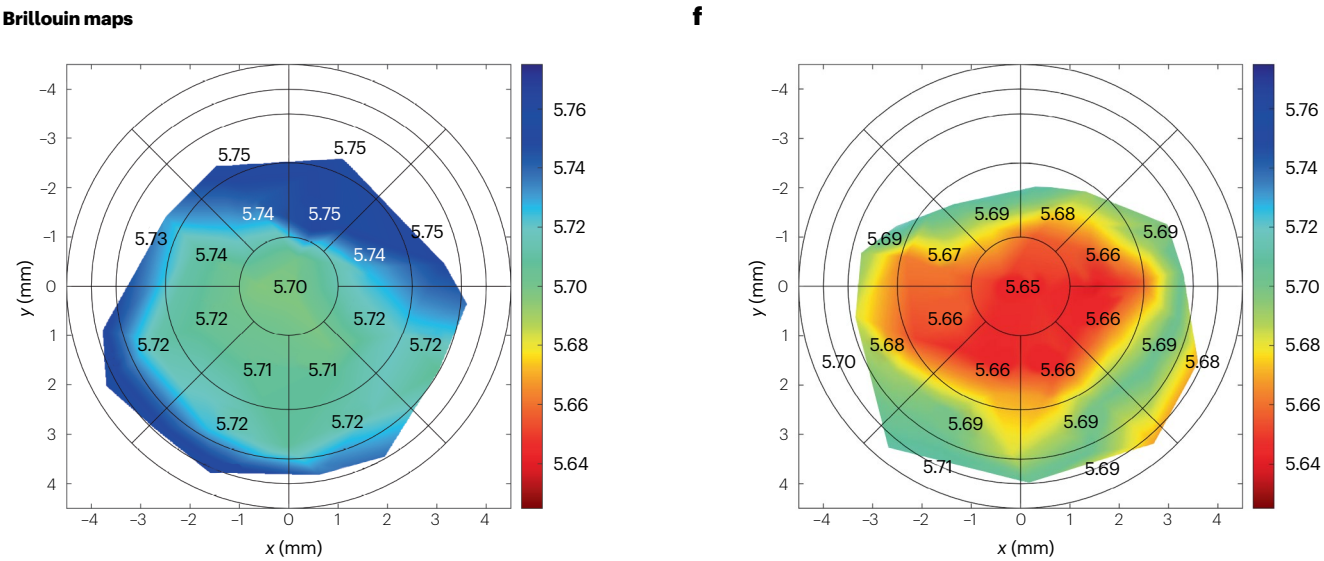

learned tools for in vivo applications. In this vein, routine use of shallow learning approaches such as the support vector machine[156] should first be adopted to assess their suitability. The corresponding hyperparameters, including the optimal classification features, can then be optimized, which will also shed light on the underlying mechanobiology and discovery of Brillouin-based biomarkers for various applications.

Fig. 8 | Application of Brillouin microscopy to ocular disease diagnostics and treatment. a, Healthy corneas have nearly spherical shape to provide needed refraction for proper vision. **b**, In keratoconus, a focal weakening of the cornea disrupts the mechanical balance with intraocular pressure (IOP), **c**, Mechanical imbalance leads to corneal thinning and bulging. **d**, Clinical instrument user interface featuring Brillouin light scattering (BLS) and 3D tracking via pupil imaging and optical coherence tomography (OCT). **e,f**, Brillouin maps for healthy (panel **e**) and keratoconus (panel **f**) corneas reveal focal weakening at an early stage. Part **d** adapted with permission from ref. 177 © The Optical Society. Parts **e** and **f** adapted with permission from ref. 132, Elsevier.

Applications

Cell mechanobiology

The importance of the mechanical interaction between biological cells and the surrounding microenvironment has now been widely recognized[157,158]. Such interaction is regulated by the mechanotransduction through which cells sense mechanical stimuli from external forces or surrounding stiffness and convert them into biochemical signalling[159]. Thus, mapping the extracellular and intracellular distribution of the elastic modulus is critical to determine the location of environmental mechanical cues as well as how forces are transmitted within a cell[160–162].

Brillouin microscopy holds great promise in mechanobiology to meet the resolution requirements for mapping mechanics at the subcellular scale as well as the experimental settings to investigate cell mechanics in 2D and 3D microenvironments, in tissues or in microfluidics platforms. To date, Brillouin microscopy has already been used to demonstrate actin polymerization and branching[22], actin remodelling[155], the correlation between intracellular modulus and cytoskeletal properties[163] as well as a cell's adhesion properties[164] and intracellular stiffness changes owing to environment perturbations[19]. At the subcellular level, Brillouin microscopy has demonstrated the ability to characterize nuclear mechanical properties[46,50,138] and the viscoelasticity of plant cells' extracellular matrix[165], and, in some cases, has even been validated by gold-standard tests and chemo-mechanical modelling[42,166]. At even higher resolution, measurements of biomolecular condensates, lipid droplets in adipocytes, and other aggregates within cells and nuclei have been recently reported[44–46,167].

Biomedical diagnostics

Ocular disease. The most mature of the applications of Brillouin microscopy is in ophthalmology, and specifically in the characterization of corneal mechanics for keratoconus and related ectatic disorders (Fig. 8). In the United States[168], keratoconus is the leading cause of corneal transplantation[169] and the most feared complication of refractive surgery, leading to post-refractive surgery corneal ectasia when undetected[170,171]. Currently, keratoconus presents clinically as a morphological disorder characterized by the thinning and increase in curvature of the cornea. However, it is widely believed that this clinical presentation is a late manifestation of the progression of the disorder, which probably starts with a mechanical degeneration of the corneal tissue[172]. Healthy corneas are mechanically strong thanks to tightly packed stromal collagen fibres which maintain shape under the outward intraocular pressure (IOP) (Fig. 8a). By contrast, keratoconic corneas have altered collagen organization[173,174] and a reduced number of cross-links[175], presenting a focal weakening[176] (Fig. 8b). Such weakening is believed to be the main driver of shape change (Fig. 8c). Brillouin microscopy is uniquely capable of measuring the loss of mechanical strength in corneas in vivo[21,132] (Fig. 8d). Recent advances in clinical instruments promise great utility in this space for keratoconus diagnostics (Fig. 8e,f), refractive surgery screening as well as therapy monitoring[177]. Within ophthalmology, another promising application of Brillouin microscopy is related to presbyopia, the loss of the dynamic vision accommodation response, which affects individuals as they age. Currently, presbyopia is treated with spectacles, which do not restore the accommodative amplitude. The issue is widely known to be caused by the stiffening of the crystalline lens leading to a strong recent effort to develop drugs that target lens biomechanics; in this respect, Brillouin microscopy has shown the ability to measure the relevant changes occurring in the lens[178], and also in clinical settings[179], and thus may represent a critical tool for drug development in this field.

Cardiovascular disease. The healthy heart functioning relies not only on the ability of its muscle fibres to contract and relax but also on maintaining the shape and structure of the organ. The way the heart muscle shortens and generates force, regardless of the existing conditions, is determined by the mechanical properties of the heart tissue[180]. When these properties are disturbed, as often happens in heart diseases, this leads to changes in the thickness of the heart's walls, stiffness of the tissue and, eventually, malfunction. However, directly assessing these properties at a local level is challenging. Brillouin microscopy was introduced to assess heart tissue's viscosity and elasticity[181]: it identified stiffness changes in healthy mouse myocardium ventricles with notably reduced stiffness in the compliant right ventricle. These results correlated strongly with speckle-tracking echocardiography, emphasizing the link between displacement and stiffness in the heart's regions[181]. In a different study, the micromechanical properties of a thin cap fibroatheroma were assessed using Brillouin microscopy[150]. A fibroatheroma is a particular stage in the progression of an atherosclerotic plaque, characterized by a thickened fibrous cap, covering a lipid-rich core[182]. Fibroatheromas are considered high-risk plaques because they have a greater likelihood of developing complications such as rupture or erosion[183]. Thus, a method for precise mechanical characterization of the fibroatheroma's stiffness and structure can prove to be invaluable for prediction of the plaque's fate. A strong inverse correlation between BFS and the local accumulation of lipid was demonstrated together with a direct relationship between frequency shift and the distribution of collagen fibres[150]. Collectively, these results support Brillouin microscopy as a method to optically measure stiffness and structural composition in atherosclerotic vessel sections.

Bone, dentin and cartilage disease. Specialized forms of connective tissue, bone and cartilage, are essential for providing structural support to muscles and organs within the human body. Their structure and mechanical properties are critical for their respective functions, whereas disruptions in these properties are associated with injuries and degenerative conditions such as arthritis and osteoporosis. Understanding of bone remodelling processes, especially in the context of implants, is limited owing to the absence of non-invasive methods to assess implant stability and osseointegration during the healing phase after implantation. The potential of Brillouin microscopy in

Glossary

Abbe diffraction limit
This determines the size of the spot to which the light can be focused based on the law of diffraction. It is approximately proportional to half of the light wavelength, setting the lower limit to the resolution of a classical optical system.

Beat signal
The wave pattern formed via interference of two waves with slightly different frequencies.

Bragg angle
The angle between the incident light beam and the diffracting grating plane.

Brillouin frequency shift
(BFS). The frequency shift that a light wave experiences undergoing Brillouin scattering process.

Elasticity tensor
A fourth-rank tensor describing the stress–strain relation in a linear elastic material. Most materials can be described as linear elastic under small deformation approximation.

Etalon
A device consisting of two reflecting glass plates, employed for measuring the light spectrum.

Longitudinal modulus
The ratio of axial stress to axial strain under confined uniaxial deformation (the object allowed to deform along one axis only, with possible changes in volume).

Matrix pencil method
A computational technique based on diagonal matrices, particularly useful to estimate parameters of complex exponential signals buried in noise.

Mechanotransduction
The conversion of an external mechanical signal into intracellular biochemical signals.

Micromechanical properties
The elastic and viscous properties of materials at the microscale.

Rayleigh band
Refers to spectral signals at and near the frequency of the laser, including Rayleigh light scattering, quasi-elastic scattering and stray laser light.

Shear modulus
The ratio of shear stress to shear strain, serving as the measure of shear stiffness.

Voxel
A measurement of volume in a structure to be imaged.

Young's modulus
A measure of the ratio of applied stress to axial strain under unconfined deformation (the object is free to deform in all directions while its volume is conserved).

distinguishing between mature and newly formed bone following implantation was recently suggested[184]. A comparative investigation between BLS and scanning acoustic microscopy was conducted to determine the sensitivity of BLS in detecting anisotropy and decalcification, hallmarks of bone diseases[185]. In a rabbit model, bone healing was quantified in terms of BFS and linewidth changes, both parameters reflecting the pace of bone generation and healing at the defect site[186]. The contribution of collagen to cartilage tissue mechanics in the regenerating axolotl model[131] and the pathogenesis of osteoarthritis and disease-related early changes in articular cartilage[36,53,81,187] have also been studied using Brillouin microscopy. Degradation of cartilage extracellular matrix typically goes hand in hand with changes in tissues' hydration, which can be traced with Brillouin microscopy with high precision[187].

Cancers and drug discovery

The mechanical properties of individual cancer cells and tumour tissue are some of the best studied topics in biomechanics. Cancer cells have almost consistently been found to be more compliant than their healthy counterparts, and increasingly so with metastatic competence[188]. This has led to the notion that the increased deformability of cancer cells is required for their migration and circulation through the body. However, to date there is no convincing evidence that this is the case. The problem is that most studies so far have been on either cell lines or cells isolated from tissues[189,190] and not on cells behaving in situ. Also, tissue mechanical measurements on the cellular scale have generally been done with excised cancer tissue biopsies[191]. This is a technological short-coming that is starting to be addressed by Brillouin microscopy[38,40]. The ability to measure single cells in complex microenvironments has enabled unique studies about the adaptability/plasticity of cell mechanical properties in different circumstances to be performed. This is particularly relevant for investigations into the metastatic cascade where the mechanical microenvironments and mechanical challenges vary significantly[192,193]. During extravasation (cells leaving the bloodstream to get into tissues), the Brillouin longitudinal modulus of cells and their nuclei was markedly lower in the transmigration phase[194], as predicted by chemo-mechanical models[195]. Ascitic fluid currents, a hallmark of poor prognosis in ovarian cancer, were shown to reduce the tumour cell modulus[196], indicating higher tumour aggressiveness. In confined migration, the nuclear modulus was inversely correlated with the confined migration speed, indicating nuclear stiffness as a critical mechanical barrier for cell motility[197].

As changes in tumour cell mechanics are required for successful metastatic capability, a promising anti-tumour strategy is to look for ways to stiffen cancer cells artificially. For this, screens of US Food and Drug Administration (FDA)-approved drug libraries or chemical compounds with a mechanical read-out of cell or nuclear stiffness could be performed. Even though Brillouin spectroscopy is relatively slow, Brillouin flow cytometry of cell nuclei at rates of 200 cells h^{-1} has already been demonstrated[166].

Tissue morphogenesis

Tissue biomechanics is deeply involved in morphogenesis[198–200]. To date, Brillouin microscopy has been used for understanding the role of mechanics in various aspects of tissue morphogenesis, including spinal cord growth and repair after injury[52], eye development[127,128], neural tube closure (NTC)[90,201], the development and regeneration of limbs[131], and early development of the kidney[202]. The model organisms analysed by Brillouin microscopy include zebrafish[52], chick[201], axolotl[131], mouse[90,202], *C. elegans*[32], *Drosophila*[37] and *Nematostella*[51].

Zebrafish are among the most common model organisms used for imaging, partly because of their optical accessibility. Using Brillouin microscopy, the tissue modulus of living zebrafish larvae in all anatomical planes has been mapped during development (3–5 days post fertilization) and after spinal cord injury[52]. The results demonstrate that Brillouin microscopy has sufficient sensitivity to distinguish the mechanical difference between tissues from distinct sites. Importantly, the results reveal that the spinal cord tissue shows a significant decrease in BFS right after injury. Moreover, the longitudinal measurement shows that the BFS of the lesion site gradually increases during the 2 days post injury but remains lower than that of adjacent uninjured tissue, which coincides with the decreased cell-body density in the lesion site.

Brillouin microscopy has also been used for quantifying tissue mechanics during NTC — a developmental process responsible for

vertebrate neurulation. If failed, it is known to be a primary cause of birth defects. Preliminary studies using co-registered Brillouin microscopy and optical coherence tomography (OCT) suggested that the BFS of the neural tube tissue of mouse embryos is higher following closure compared with when it is open[90,203]. Recently, time-lapse Brillouin imaging of neural tube tissue during NTC was conducted by combining confocal Brillouin microscope with a modified ex ovo culture of chick embryos[201]. The longitudinal experiment observes the increasing BFS and thickness of the neural tube during NTC, which is concurrent with the bending of the neural plate. This study provides a platform for further understanding the underlying cellular and molecular mechanisms that regulate the procedure of NTC as well as neural tube defects.

In addition, Brillouin microscopy has been employed to understand the role of biomechanics in the packing of tip domains for early development of the kidney using a mouse model[202]. Results show a strong correlation between cap mesenchyme cell BFS and geometric patterning, suggesting mechanical changes during branching and expansion. Early nephrons appear to have higher BFS than cap mesenchymal cells.

3D bioprinting and tissue engineering

The advent of 3D bioprinting has transformed biofabrication, providing an accurate, cost-efficient and relatively straightforward approach for creating in vitro living systems on a large scale[204,205]. Quality control is vital, owing to complex designs of bioprinted constructs. Brillouin microscopy presents a promising avenue for assessing the micromechanical properties of bioprinted models, either during or post fabrication[73]. Complex hydrogel structures created through drop-on-demand bioprinting were imaged using Brillouin microscopy showing high sensitivity to small (5%) variations in the gel's cross-linking and solid component[57]. This study also identified non-uniform distribution of mechanical properties across 3D prints despite constant printing conditions as the result of a non-homogeneous cross-linking process and non-uniform hydrogel swelling[57]. 3D mapping of micromechanical properties is also attractive for the development of artificial tissue models aimed at tissue regeneration applications in spinal cord injury and heart disease[54,73]. Both pathologies lead to fundamental alteration of mechanical properties in native tissues through formation of fibrous scarring, leading to the patient's disability or organ failure. Brillouin microscopy was successfully utilized for characterization of 3D bioprinted neural cell models[73] and cardiac spheroids[54], helping assess the models' long-term mechanical stability under physiological conditions.

Reproducibility and data deposition

The reproducibility and data quality of Brillouin spectra can be influenced by various factors. The principal factors together with the best practices for mitigating these effects are discussed below.

Factors affecting reproducibility

Modifications and variability in sample viscoelastic properties. The mechanical properties of viscoelastic materials depend on the physical conditions of the samples, such as temperature, hydration and pressure. Moreover, the mechanical properties are frequency dependent; thus, to compare the measurements obtained in different laboratories, the chosen experimental conditions, together with the power and laser frequency, must be clearly indicated. High-power continuous-wave illumination (>200 mW) in semi-transparent samples can lead to thermal effects, especially for the illumination wavelengths outside the biological transparency window (600–800 nm). Such prolonged exposures could cause the local temperature to rise[97], but the BFS caused by thermal effects is insignificant (at lower powers and for 530–800 nm laser wavelength) as it falls well below the measurement spectral precision.

When the investigation includes complex biological samples such as cells and tissues, statistical analysis is needed. Acquiring a large number of spectra on multiple samples is necessary to estimate the confidence of the results, considering the biological variability.

The optical layout chosen to acquire Brillouin spectra. The optical configuration, including the scattering geometry, affects the final shape and position of the Brillouin spectra. The modifications are particularly relevant in microscopy arrangements using high NA objectives. In this case, the spread in the collected exchanged wave vector, **q**, can modify the position and the linewidth of the Brillouin peak. To extract the relevant parameters from the spectrum, the measure or the theoretical evaluation of the **q**-spread has to be used to de-convolve the raw data.

The use of different Brillouin spectrometers. The spectral resolution and contrast of the spectrometer/interferometer can modify the measured spectra in terms of the SNR and line shape. For isotropic samples, the deconvolution with the response function of the spectrometers has to be used to obtain the corrected values of Ω_B and Γ. In general, to account for the spread in the collected exchanged wave vector **q** and the finite spectral resolution of the spectrometer, the spectrum of a material with a negligible intrinsic broadening, with an expected Brillouin peak approximal to a Dirac delta function (for example, vitreous silica), can be used for the direct evaluation of the Brillouin set-up response.

Data deposition

Although the standard unit in the reporting of BFS has been proposed[15], the standardization in the data treatment and the creation of data repositories remains a challenge in the bio-Brillouin field. To date, Brillouin spectroscopy applied to biological samples is still not used routinely and most laboratories put together home-built set-ups in which the frequency response, the spectral resolution and the contrast are characteristics of each individual system. Additionally, different models are currently used to fit the Brillouin spectra. The importance of the standardization of the data treatment and the creation of a data repository was recently highlighted in the community, and is one of the main goals for the newly founded Bio-Brillouin Society. The Bio-Brillouin Society is working to build the first repository for raw Brillouin data acquired on simple samples by the different set-ups. The required information is the wavelength of the laser beam, the scattering geometry and the used set-up. Moreover, the laser power, the sample condition (such as temperature and hydration) and the microscope objective should be specified in order to obtain comparable data.

Limitations and optimizations

The first obstacle towards wide adoption of Brillouin microscopy is the slow acquisition time compared with other microscopy techniques. Spontaneous Brillouin microscopy is now close to the fundamental limit set by the weak interaction strength between incident photons and thermal phonons inside the medium; further improvements in imaging speed can be achieved with multiplexing speed[37,39]. In non-linear Brillouin scattering, much stronger Brillouin signals are available because two light beams drive material phonon excitation which, in turn, scatters light efficiently. Non-linear Brillouin technologies are

established in material research and several laboratories have now translated stimulated Brillouin scattering (SBS) to biomedicine with frequency-domain or time-domain approaches. However, current SBS spectrometers have not provided dramatic speed-up for biomedical measurements so far because of small interaction volumes and photodamage limits as well as the lack of suitable sources for SBS in biological media. Improving on SBS performance represents a great opportunity for the field to grow.

Instrumentation, cost, size and complexity of operation are also a significant hurdle for widespread adoption. The currently used spontaneous Brillouin microscopes cost more than US$100,000 to run, occupy an optical table and are sophisticated instruments to operate at peak performance; SBS microscopes may be even more costly and complex to optimize and operate given the double-access alignment requirements. On this front, several companies are trying to overcome the issue and individual laboratories are aiming to make intuitive software and alignment protocol instructions more readily available and accessible to non-experts[84,133]. Advances in nanofabrication and optical fibre technology can help reduce the complexity and footprint of Brillouin systems further, as recently demonstrated for fibre-integrated Brillouin imaging[206] and chip-based laser light filtering[207].

Brillouin microscopy is currently under-utilized as a label-free technique providing mechanical contrast. The scientific reason behind this is probably the unconventional nature of the mechanical information compared with gold-standard biomechanical measurements. The high-frequency longitudinal modulus[46] occupies a different scale of magnitude values compared with the traditional Young's modulus, which can be confusing for end users and can generate scepticism. Interestingly, this challenge has spurred high-quality research in the past decade, focusing on the fundamental relation between traditional and Brillouin mechanical signatures that goes beyond the empirical correlations used in early studies[117,120]; the search for the biological determinants of Brillouin mechanical signatures; and a direct connection between Brillouin signature and end-user diagnostic applications, which in some fields, for example ophthalmology, has provided remarkable success in the clinic[132,208].

Brillouin microscopy is highly directional, probing the axis of the modulus in the same direction of the light (in a traditional epi-detection configuration). On the one hand, this means that uniquely Brillouin microscopy can characterize the full elastic modulus tensor in anisotropic materials[25,134,135]; on the other, in anisotropic biological materials, mapping only one axis – as in the majority of Brillouin biological studies demonstrated to date – does not provide a comprehensive characterization and may actually provide confusing results. This is only a technical challenge for the field; once the speed of the instruments grows, being able to create multiple maps at different angles will become feasible within practical experimental settings.

Outlook

Exploiting the optical advantage

Brillouin microscopy's biggest advantage, which it shares with other forms of optical elastography[48], is that it is an optical technique that permits the quantitative exploration of material properties inside cells, tissues and organisms. This is an option not previously available with other more traditional methods to measure mechanical properties in biology[209]. Whereas Brillouin microscopy exploits the inherent, thermally driven density fluctuations, other optical elastography techniques externally apply a known, often oscillatory deformation at given frequencies. This has important consequences. The option to choose excitation frequencies means that the mechanical response can be tested in a shear mode and on timescales that are closer to those commonly used in non-optical techniques, such as AFM nanoindentation (0.1–10 kHz), which is far away from the gigahertz frequencies relevant in Brillouin microscopy. On the other hand, gigahertz frequencies translate to higher spatial, subcellular resolution, whereas other optical techniques often struggle to achieve even cellular resolution. It is this high spatial resolution that permits the investigation of intracellular mechanical heterogeneities. In particular, nuclear mechanics measured inside intact cells is hardly possible with other means, and very important in the context of cell migration in confined spaces where nuclear deformability is the rate-limiting factor. Also, the dynamic mechanical changes of immune and cancer cells during transendothelial and interstitial migration in situ can now be quantified with important implications for better understanding of the immune response and cancer metastasis. As a new and emerging topic, the increased deformability of cancer cells seems not only relevant for migration but also as an immune escape mechanism. In this context, Brillouin microscopy will be an important tool to study the mechanical interaction between cancer and immune cells at the immune synapse.

Brillouin microscopy for mechanosensing

In the wider context of biological application, the use of Brillouin microscopy will increasingly move away from demonstrating its general applicability for all kinds of cells, tissues and organisms and towards answering biologically relevant questions in morphogenesis, development and pathology. An exciting example could be investigating the role of mechanosensing during spinal cord repair. The use of zebrafish larvae is beneficial in this context because of their high optical transparency, which is particularly important for Brillouin microscopy, and because they can actually repair an injury to their spinal cord within days[52]. Insight into these mechanisms could help cure spinal cord injuries also in mammals, which is currently not possible. Of course, the likely mode of cells mechanically testing their environment is a shear deformation on timescales of milliseconds to seconds, which renders Brillouin microscopy seemingly less ideal for studies into mechanosensing. Also, the correlation frequently observed between the longitudinal modulus measured with Brillouin microscopy and the Young's modulus obtained with AFM nanoindentation probably holds only in the same type of material. What if the structural basis for the mechanical properties changes within tissues, for example from cell-body dominated to extracellular matrix dominated? Even though not yet demonstrated, it might be possible to address these challenges by using machine learning together with employing other measurement modalities simultaneously, such as fluorescence or Raman imaging in order to obtain sufficient additional information about the tissues. Transferring this learning, it might be possible to reliably infer AFM-type shear modulus information at timescales of seconds from Brillouin frequency maps obtained in areas not accessible to AFM.

Quantifying emergent biophysical phenomena

Finally, it might also be time to emancipate the field of Brillouin microscopy from the attempt to provide the kind of information conventionally obtained by other contact-based methods (such as AFM nanoindentation). After all, there should be significance in the fact that tissues are naturally excited at gigahertz frequencies by thermal excitation. It seems unlikely that this aspect had been excluded from evolutionary optimization and is not somehow utilized by cells. Looking at the amplitudes of the density fluctuations involved, which are on the

scale of nanometres, it is only natural to suggest that Brillouin microscopy might be sensitive to intermolecular interactions. How strongly molecules interact with each other is a very relevant question across all of molecular biology, particularly biomolecular condensates[167]. Certain proteins condense to form liquid droplets inside cells. This is a biologically regulated process, likely to sequester these proteins away from other reactions going on in the cell, or to locally increase their concentration beyond a critical point to enable certain reactions. The interaction of these molecules must be so specific that only certain proteins form condensates, but without proceeding to crystallization. The molecular grammar involved in these condensation phenomena is currently being deciphered. This is an area where Brillouin microscopy, with its sensitivity for intermolecular interactions, could be the label-free, quantitative and direct measurement technique needed to take this field forward. Brillouin microscopy has already demonstrated that it can detect and analyse the properties of protein condensates inside living cells[44]. Interestingly, mutations in some of the proteins known to form biomolecular condensates, such as fused in sarcoma proteins, are linked to neurodegenerative disorders such as amyotrophic lateral sclerosis[210]. Mutations also cause an irreversible phase transition of the condensates from a liquid to a solid state. At present, it is not clear whether, and if so how, this change in material properties of the condensates is causally linked to disease pathogenesis, but considering the plaques found in the end states of the disease, it seems sensible to look for such a connection. Brillouin microscopy will have a role to play in this quest. More generally, with the molecular level of biology starting to be very well investigated, there is the question of how the genomic, proteomic, transcriptomic molecular information is used and how this level of information can be conceptionally transferred to larger scales. Some aspect of the solution will involve the self-organization of proteins and so on at supramolecular, subcellular scales. Again, Brillouin microscopy seems ideally suited to contribute to the quantitative exploration of these emergent properties and to drive the paradigm shift in biology from the biochemistry of molecules to the next level. In summary, the future of Brillouin microscopy looks bright.

Published online: 01 February 2024

References

1. Wolff, J., *Das Gesetz der Transformation der Knochen* [German] (Hirschwald, 1892).
2. Ingber, D. Mechanobiology and diseases of mechanotransduction. *Ann. Med.* **35**, 564–577 (2003).
3. Keller, R. Physical biology returns to morphogenesis. *Science* **338**, 201–203 (2012).
4. Baratchi, S. et al. Molecular sensors of blood flow in endothelial cells. *Trends Mol. Med.* **23**, 850–868 (2017).
5. Kalli, M. & Stylianopoulos, T. Defining the role of solid stress and matrix stiffness in cancer cell proliferation and metastasis. *Front. Oncol.* **8**, 55 (2018).
6. Urbanska, M. et al. A comparison of microfluidic methods for high-throughput cell deformability measurements. *Nat. Methods* **17**, 587–593 (2020).
7. Arbore, C. et al. Probing force in living cells with optical tweezers: from single-molecule mechanics to cell mechanotransduction. *Biophys. Rev.* **11**, 765–782 (2019).
8. Wang, H. et al. Recent advances of optical tweezers-based dynamic force spectroscopy and mechanical measurement assays for live-cell mechanobiology. *Front. Phys.* **10**, 1–11 (2022).
9. Staunton, J. R. et al. Correlating confocal microscopy and atomic force indentation reveals metastatic cancer cells stiffen during invasion into collagen I matrices. *Sci. Rep.* **6**, 19686 (2016).
10. Benitez, R. & Toca-herrera, J. L. Looking at cell mechanics with atomic force microscopy: experiment and theory. *Microsc. Res. Tech.* **77**, 947–958 (2014).
11. Li, Y. et al. Ultrahigh-sensitive optical coherence elastography. *Light Sci. Appl.* **9**, 58 (2020).
12. Scarcelli, G. & Yun, S. H. Confocal Brillouin microscopy for three-dimensional mechanical imaging. *Nat. Photonics* **2**, 39–43 (2008).
13. Poon, C. et al. Brillouin imaging for studies of micromechanics in biology and biomedicine: from current state-of-the-art to future clinical translation. *J. Phys. Photonics* **3**, 012002 (2021).
14. Prevedel, R. et al. Brillouin microscopy: an emerging tool for mechanobiology. *Nat. Methods* **16**, 969–977 (2019).
15. Antonacci, G. et al. Recent progress and current opinions in Brillouin microscopy for life science applications. *Biophys. Rev.* **12**, 615–624 (2020).
16. Matsuda, O. et al. Fundamentals of picosecond laser ultrasonics. *Ultrasonics* **56**, 3–20 (2015).
17. Tomoda, M. et al. Time-domain Brillouin imaging of sound velocity and refractive index using automated angle scanning. *Photoacoustics* **31**, 100486 (2023).
18. Gusev, V. & Ruello P. Advances in applications of time-domain Brillouin scattering for nanoscale imaging. *Appl. Phys. Rev.* **5**, 031101 (2018).
19. Conrad, C. et al. Mechanical characterization of 3D ovarian cancer nodules using Brillouin confocal microscopy. *Cell. Mol. Bioeng.* **12**, 215–226 (2019).
20. Bevilacqua, C. et al. Imaging mechanical properties of sub-micron ECM in live zebrafish using Brillouin microscopy. *Biomed. Opt. Express* **10**, 1420–1431 (2019).
21. Scarcelli, G. et al. In vivo biomechanical mapping of normal and keratoconus corneas. *JAMA Ophthalmol.* **133**, 480–482 (2015).
22. Scarcelli, G. et al. Noncontact three-dimensional mapping of intracellular hydromechanical properties by Brillouin microscopy. *Nat. Methods* **12**, 1132–1134 (2015).
23. Fiore, A., Bevilacqua, C. & Scarcelli, G. Direct three-dimensional measurement of refractive index via dual photon-phonon scattering. *Phys. Rev. Lett.* **122**, 103901 (2019).
24. Chan, C. J., Bevilacqua, C. & Prevedel, R. Mechanical mapping of mammalian follicle development using Brillouin microscopy. *Commun. Biol.* **4**, 1133 (2021).
25. Palombo, F. et al. Biomechanics of fibrous proteins of the extracellular matrix studied by Brillouin scattering. *J. Royal Soc. Interface* **11**, 20140739 (2014).
26. Bottani, C. E. & Fioretto, D. Brillouin scattering of phonons in complex materials. *Adv. Phys.: X* **3**, 1467281 (2018).
27. Merklein, M. et al. 100 years of Brillouin scattering: historical and future perspectives. *Appl. Phys. Rev.* **9**, 041306 (2022).
28. Kim, M. et al. Shear Brillouin light scattering microscope. *Opt. Express* **24**, 319–328 (2016).
29. Fioretto, D. et al. Cauchy relation in relaxing liquids. *J. Chem. Phys.* **128**, 214502 (2008).
30. Cusack, S. & Miller, A. Determination of the elastic constants of collagen by Brillouin light scattering. *J. Mol. Biol.* **135**, 39–51 (1979).
31. Koski, K. J. et al. Non-invasive determination of the complete elastic moduli of spider silks. *Nat. Mater.* **12**, 262–267 (2013).
32. Remer, I. et al. High-sensitivity and high-specificity biomechanical imaging by stimulated Brillouin scattering microscopy. *Nat. Methods* **17**, 913–916 (2020).
33. Ballmann, C. W. et al. Stimulated Brillouin scattering microscopic imaging. *Sci. Rep.* **5**, 18139 (2015).
34. Mock, R., Hillebrands, B. & Sandercock, R. Construction and performance of a Brillouin scattering set-up using a triple-pass tandem Fabry–Perot interferometer. *J. Phys. E Sci. Instruments* **20**, 656 (1987).
35. Shirasaki, M. Large angular dispersion by a virtually imaged phased array and its application to a wavelength demultiplexer. *Opt. Lett.* **21**, 366–368 (1996).
36. Alunni Cardinali, M. et al. Brillouin–Raman microspectroscopy for the morpho-mechanical imaging of human lamellar bone. *J. R. Soc. Interface* **19**, 20210642 (2022).
37. Bevilacqua, C. et al. High-resolution line-scan Brillouin microscopy for live imaging of mechanical properties during embryo development. *Nat. Methods* **20**, 755–760 (2023).
38. Margueritat, J. et al. High-frequency mechanical properties of tumors measured by Brillouin light scattering. *Phys. Rev. Lett.* **122**, 018101 (2019).
39. Zhang, J. et al. Rapid biomechanical imaging at low irradiation level via dual line-scanning Brillouin microscopy. *Nat. Methods* **20**, 677–681 (2023).
40. Mahajan, V. et al. Mapping tumor spheroid mechanics in dependence of 3D microenvironment stiffness and degradability by Brillouin microscopy. *Cancers* **13**, 5549 (2021).
41. Karampatzakis, A. et al. Probing the internal micromechanical properties of *Pseudomonas aeruginosa* biofilms by Brillouin imaging. *NPJ Biofilms Microbiomes* **3**, 20 (2017).
42. Zhang, J. et al. Nuclear mechanics within intact cells is regulated by cytoskeletal network and internal nanostructures. *Small* **16**, 1907688 (2020).
43. Bacete, L. et al. THESEUS1 modulates cell wall stiffness and abscisic acid production in *Arabidopsis thaliana*. *Proc. Natl Acad. Sci. USA* **119**, e2119258119 (2022).
44. Antonacci, G. et al. Background-deflection Brillouin microscopy reveals altered biomechanics of intracellular stress granules by ALS protein FUS. *Commun. Biol.* **1**, 139 (2018).
45. Fasciani, A. et al. MLL4-associated condensates counterbalance Polycomb-mediated nuclear mechanical stress in Kabuki syndrome. *Nat. Genet.* **52**, 1397–1411 (2020).
46. Schlüßler, R. et al. Correlative all-optical quantification of mass density and mechanics of subcellular compartments with fluorescence specificity. *eLife* **11**, e68490 (2022).
47. Shao, P. et al. Spatially-resolved Brillouin spectroscopy reveals biomechanical abnormalities in mild to advanced keratoconus in vivo. *Sci. Rep.* **9**, 7467 (2019).
48. Kennedy, B. F., Wijesinghe, P. & Sampson, D. D. The emergence of optical elastography in biomedicine. *Nat. Photonics* **11**, 215–221 (2017).
49. Olie, C. S. et al. Cytoskeletal disorganization underlies PABPN1-mediated myogenic disability. *Sci. Rep.* **10**, 17621 (2020).
50. Frittoli, E. et al. Tissue fluidification promotes a cGAS–STING cytosolic DNA response in invasive breast cancer. *Nat. Mater.* **22**, 644–655 (2022).

51. Pukhlyakova, E. et al. β-Catenin-dependent mechanotransduction dates back to the common ancestor of Cnidaria and Bilateria. *Proc. Natl Acad. Sci. USA* **115**, 6231–6236 (2018).
52. Schlüßler, R. et al. Mechanical mapping of spinal cord growth and repair in living zebrafish larvae by Brillouin imaging. *Biophys. J.* **115**, 911–923 (2018).
53. Bailey, M. et al. Viscoelastic properties of biopolymer hydrogels determined by Brillouin spectroscopy: a probe of tissue micromechanics. *Sci. Adv.* **6**, eabc1937 (2020).
54. Polonchuk, L. et al. Towards engineering heart tissues from bioprinted cardiac spheroids. *Biofabrication* **13**, 045009 (2021).
55. Pagano, S. et al. Bio-mechanical characterization of a CAD/CAM PMMA resin for digital removable prostheses. *Dental Mater.* **37**, e118–e130 (2021).
56. Lainović, T. et al. Micromechanical imaging of dentin with Brillouin microscopy. *Acta Biomaterialia* **105**, 214–222 (2020).
57. Mahmodi, H. et al. Mechanical mapping of bioprinted hydrogel models by Brillouin microscopy. *Bioprinting* **23**, e00151 (2021).
58. Mattarelli, M., Vassalli, M. & Caponi, S. Relevant length scales in Brillouin imaging of biomaterials: the interplay between phonons propagation and light focalization. *ACS Photonics* **7**, 2319–2328 (2020).
59. Passeri, A. A. et al. Size and environment: the effect of phonon localization on micro-Brillouin imaging. *Biomater. Adv.* **147**, 213341 (2023).
60. Caponi, S., Fioretto, D. & Mattarelli, M. On the actual spatial resolution of Brillouin imaging. *Opt. Lett.* **45**, 1063–1066 (2020).
61. Mattarelli, M. et al. Vibration spectroscopy of weakly interacting mesoscopic colloids. *Soft Matter* **8**, 4235–4243 (2012).
62. Still, T. et al. Eigenvibrations of submicrometer colloidal spheres. *J. Phys. Chem. Lett.* **1**, 2440–2444 (2010).
63. Gomopoulos, N. et al. Out-of-plane longitudinal elastic modulus of supported polymer thin films. *Macromolecules* **42**, 7164–7167 (2009).
64. Kabakova, I., Scarcelli, G. & Yun, S.-H. in *Semiconductors and Semimetals* Ch. 15 (eds Eggleton, B. J., Steel, M. J. & Poulton, C. G.) 313–348 (Elsevier, 2022).
65. Remer, I. & Bilenca, A. High-speed stimulated Brillouin scattering spectroscopy at 780 nm. *APL Photonics* **1**, 061301 (2016).
66. Shaashoua, R. et al. Brillouin gain microscopy. Preprint at https://doi.org/10.48550/arXiv.2306.00889 (2023).
67. Chow, D. M. & Yun, S.-H. Pulsed stimulated Brillouin microscopy. *Opt. Express* **31**, 19818–19827 (2023).
68. Lindsay, S., Anderson, M. & Sandercock, J. Construction and alignment of a high performance multipass vernier tandem Fabry–Perot interferometer. *Rev. Sci. Instrum.* **52**, 1478–1486 (1981).
69. Dil, J. G. Brillouin scattering in condensed matter. *Rep. Prog. Phys.* **45**, 285–334 (1982).
70. Hickman, G. D. et al. Aircraft laser sensing of sound velocity in water: Brillouin scattering. *Remote sensing Environ.* **36**, 165–178 (1991).
71. Harley, R. et al. Phonons and the elastic moduli of collagen and muscle. *Nature* **267**, 285–287 (1977).
72. Randall, J. T. & Vaughan, J. M. Brillouin scattering in systems of biological significance. *Philos. Trans. Royal Soc. Lond. Series A, Math. Phys. Sci.* **293**, 341–348 (1979).
73. Rad, M. A. et al. Micromechanical characterisation of 3D bioprinted neural cell models using Brillouin microspectroscopy. *Bioprinting* **25**, e00179 (2022).
74. Vaughan, J. & Randall, J. Brillouin scattering, density and elastic properties of the lens and cornea of the eye. *Nature* **284**, 489–491 (1980).
75. Randall, J. & Vaughan, J. The measurement and interpretation of Brillouin scattering in the lens of the eye. *Proc. Royal Soc. Lond. B: Biol. Sci.* **214**, 449–470 (1982).
76. Mercatelli, R. et al. Morpho-mechanics of human collagen superstructures revealed by all-optical correlative micro-spectroscopies. *Commun. Biol.* **2**, 117 (2019).
77. Lee, S. et al. A Brillouin scattering study of the hydration of Li- and Na-DNA films. *Biopolymers: Original Res. Biomolecules* **26**, 1637–1665 (1987).
78. Scarponi, F. et al. High-performance versatile setup for simultaneous Brillouin–Raman microspectroscopy. *Phys. Rev. X* **7**, 031015 (2017).
79. Itoh, S.-I., Yamana, T. & Kojima, S. Quick measurement of Brillouin spectra of glass-forming material trimethylene glycol by angular dispersion-type Fabry–Perot interferometer system. *Japanese J.Appl. Phys.* **35**, 2879 (1996).
80. Cardinali, M. A. et al. Mechano-chemistry of human femoral diaphysis revealed by correlative Brillouin–Raman microspectroscopy. *Sci. Rep.* **10**, 17341 (2020).
81. Cardinali, M. A. et al. Brillouin micro-spectroscopy of subchondral, trabecular bone and articular cartilage of the human femoral head. *Biomed. Opt. Express* **10**, 2606–2611 (2019).
82. Koski, K. J. & Yarger, J. L. Brillouin imaging. *Appl. Phys. Lett.* **87**, 061903 (2005).
83. Scarcelli, G. & Yun, S. H. Multistage VIPA etalons for high-extinction parallel Brillouin spectroscopy. *Opt. Express* **19**, 10913–10922 (2011).
84. Berghaus, K. V., Yun, S. H. & Scarcelli, G. High speed sub-GHz spectrometer for Brillouin scattering analysis. *J. Vis. Exp.* **106**, e53468 (2015).
85. Antonacci, G. et al. Elastic suppression in Brillouin imaging by destructive interference. *Appl. Phys. Lett.* **107**, 061102 (2015).
86. Fiore, A. et al. High-extinction virtually imaged phased array-based Brillouin spectroscopy of turbid biological media. *Appl. Phys. Lett.* **108**, 203701 (2016).
87. Edrei, E., Gather, M. C. & Scarcelli, G. Integration of spectral coronagraphy within VIPA-based spectrometers for high extinction Brillouin imaging. *Opt. Express* **25**, 6895–6903 (2017).
88. Nikolić, M. & Scarcelli, G. Long-term Brillouin imaging of live cells with reduced absorption-mediated damage at 660 nm wavelength. *Biomed. Optics Exp.* **10**, 1567–1580 (2019).
89. Raghunathan, R. et al. Evaluating biomechanical properties of murine embryos using Brillouin microscopy and optical coherence tomography. *J. Biomed. Opt.* **22**, 086013 (2017).
90. Zhang, J. et al. Tissue biomechanics during cranial neural tube closure measured by Brillouin microscopy and optical coherence tomography. *Birth Defects Res.* **111**, 991–998 (2018).
91. Huisken, J. et al. Optical sectioning deep inside live embryos by selective plane illumination microscopy. *Science* **305**, 1007–1009 (2004).
92. Stelzer, E. H. et al. Light sheet fluorescence microscopy. *Nat. Rev. Methods Primers* **1**, 73 (2021).
93. Zhang, J. et al. Line-scanning Brillouin microscopy for rapid non-invasive mechanical imaging. *Sci. Rep.* **6**, 35398 (2016).
94. Remer, I., Cohen, L. & Bilenca, A. High-speed continuous-wave stimulated Brillouin scattering spectrometer for material analysis. *J. Vis. Exp.* **127**, e55527 (2017).
95. Faris, G. W., Jusinski, L. E. & Hickman, A. P. High-resolution stimulated Brillouin gain spectroscopy in glasses and crystals. *J. Opt. Soc. Am. B* **10**, 587–599 (1993).
96. Ratanaphruks, K., Tandy Grubbs, W. & MacPhail, R. A. cw stimulated Brillouin gain spectroscopy of liquids. *Chem. Phys. Lett.* **182**, 371–378 (1991).
97. Taylor, M. A. et al. Heterodyne Brillouin microscopy for biomechanical imaging. *Biomed. Opt. Exp.* **12**, 6259–6268 (2021).
98. Shaashoua, R. et al. Enhancing biomechanical stimulated Brillouin scattering imaging with physics-driven model selection. Preprint at https://doi.org/10.48550/arXiv.2306.00910 (2023).
99. Shaashoua, R. & Bilenca, A. Aperture-induced spectral effects in stimulated Brillouin scattering microscopy. *Appl. Phys. Lett.* **122**, 143702 (2023).
100. Li, T. et al. Quantum-enhanced stimulated Brillouin scattering spectroscopy and imaging. *Optica* **9**, 959–964 (2022).
101. Yang, F. et al. Pulsed stimulated Brillouin microscopy enables high-sensitivity mechanical imaging of live and fragile biological specimens. *Nat. Methods* **20**, 1971–1979 (2023).
102. Ballmann, C. W. et al. Impulsive Brillouin microscopy. *Optica* **4**, 124–128 (2017).
103. Li, J. et al. High-speed non-contact measurement of elasto-optic coefficient via laser-induced phonons. *Appl. Phys. Lett.* **121**, 251102 (2022).
104. Krug, B. et al. Nonlinear microscopy using impulsive stimulated Brillouin scattering for high-speed elastography. *Opt. Express* **30**, 4748–4758 (2022).
105. Krug, B., Koukourakis, N. & Czarske, J. W. Impulsive stimulated Brillouin microscopy for non-contact, fast mechanical investigations of hydrogels. *Opt. Express* **27**, 26910–26923 (2019).
106. Maznev, A. A., Nelson, K. A. & Rogers, J. A. Optical heterodyne detection of laser-induced gratings. *Opt. Lett.* **23**, 1319–1321 (1998).
107. Kinoshita, S. et al. New high-resolution phonon spectroscopy using impulsive stimulated Brillouin scattering. *Rev. Sci. Instrum.* **64**, 3384–3393 (1993).
108. Nelson, K. A. & Fayer, M. D. Laser induced phonons: a probe of intermolecular interactions in molecular solids. *J. Chem. Phys.* **72**, 5202–5218 (2008).
109. Erdogan, T. & Mizrahi, V. Thin-film filters come of age. *Photonics Spectra* **37**, 94–100 (2003).
110. Meng, Z., Traverso, A. J. & Yakovlev, V. V. Background clean-up in Brillouin microspectroscopy of scattering medium. *Opt. Express* **22**, 5410–5415 (2014).
111. Lepert, G. et al. Assessing corneal biomechanics with Brillouin spectro-microscopy. *Faraday Discuss* **187**, 415–428 (2016).
112. Berghaus, K. et al. High-finesse sub-GHz-resolution spectrometer employing VIPA etalons of different dispersion. *Opt. Lett.* **40**, 4436–4439 (2015).
113. Correa, N. et al. Image analysis applied to Brillouin images of tissue-mimicking collagen gelatins. *Biomed. Opt. Express* **10**, 1329–1338 (2019).
114. Hauck, N. et al. PNIPAAm microgels with defined network architecture as temperature sensors in optical stretchers. *Mater. Adv.* **3**, 6179–6190 (2022).
115. Girardo, S. et al. Standardized microgel beads as elastic cell mechanical probes. *J. Mater. Chem. B* **6**, 6245–6261 (2018).
116. Hauck, N. et al. Droplet-assisted microfluidic fabrication and characterization of multifunctional polysaccharide microgels formed by multicomponent reactions. *Polymers* **10**, 1055 (2018).
117. Wu, P.-J. et al. Water content, not stiffness, dominates Brillouin spectroscopy measurements in hydrated materials. *Nat. Methods* **15**, 561–562 (2018).
118. Zhao & Vanderwal, J. J. Brillouin scattering study of gelatin gel. *Polym. Gels Netw.* **5**, 23–36 (1997).
119. Johnson, D. L. Elastodynamics of gels. *J. Chem. Phys.* **77**, 1531–1539 (1982).
120. Scarcelli, G. & Yun, S. H. Reply to 'Water content, not stiffness, dominates Brillouin spectroscopy measurements in hydrated materials'. *Nat. Methods* **15**, 562–563 (2018).
121. Shao, P. et al. Effects of corneal hydration on Brillouin microscopy in vivo. *Invest. Ophthalmol. Vis. Sci.* **59**, 3020–3027 (2018).
122. Scarcelli, G. et al. Brillouin microscopy of collagen crosslinking: noncontact depth-dependent analysis of corneal elastic modulus. *Invest. Ophthalmol. Vis. Sci.* **54**, 1418–1425 (2013).
123. Scarcelli, G., Kim & Yun, S. H. In vivo measurement of age-related stiffening in the crystalline lens by Brillouin optical microscopy. *Biophys. J.* **101**, 1539–1545 (2011).
124. Scarcelli, G., Pineda, R. & Yun, S. H. Brillouin optical microscopy for corneal biomechanics. *Invest. Ophthalmol. Vis. Sci.* **53**, 185–190 (2012).

125. Gouveia, R. M. et al. Assessment of corneal substrate biomechanics and its effect on epithelial stem cell maintenance and differentiation. *Nat. Commun.* **10**, 1496 (2019).
126. Weber, I. P. et al. The role of cell body density in ruminant retina mechanics assessed by atomic force and Brillouin microscopy. *Phys. Biol.* **14**, 065006 (2017).
127. Amini, R. et al. Amoeboid-like migration ensures correct horizontal cell layer formation in the developing vertebrate retina. *eLife* **11**, e76408 (2022).
128. Soans, K. G. et al. Collective cell migration during optic cup formation features changing cell–matrix interactions linked to matrix topology. *Curr. Biol.* **32**, 4817–4831.e9 (2022).
129. Sánchez-Iranzo, H. et al. A 3D Brillouin microscopy dataset of the in-vivo zebrafish eye. *Data Brief* **30**, 105427 (2020).
130. Ryu, S. et al. Label-free histological imaging of tissues using Brillouin light scattering contrast. *Biomed. Opt. Express* **12**, 1437–1448 (2021).
131. Riquelme-Guzmán, C. et al. In vivo assessment of mechanical properties during axolotl development and regeneration using confocal Brillouin microscopy. *Open Biol.* **12**, 220078 (2022).
132. Zhang, H. et al. Motion tracking Brillouin microscopy evaluation of normal, keratoconic, and post-laser vision correction corneas. *Am. J. Ophthalmol.* **254**, 128–140 (2023).
133. Zhang, J. & Scarcelli, G. Mapping mechanical properties of biological materials via an add-on Brillouin module to confocal microscopes. *Nat. Protocols* **16**, 1251–1275 (2021).
134. Webb, J. N. et al. Detecting mechanical anisotropy of the cornea using Brillouin microscopy. *Transl. Vis. Science Technol.* **9**, 26–26 (2020).
135. Eltony, A. M., Shao, P. & Yun, S. H. Measuring mechanical anisotropy of the cornea with Brillouin microscopy. *Nat. Commun* **13**, 1354 (2022).
136. Griffith, L. G. & Swartz, M. A. Capturing complex 3D tissue physiology in vitro. *Nat. Rev. Mol. Cell Biol.* **7**, 211–224 (2006).
137. Nikolić, M., Scarcelli, G. & Tanner, K. Multimodal microscale mechanical mapping of cancer cells in complex microenvironments. *Biophys. J.* **121**, 3586–3599 (2022).
138. Bakhshandeh, S. et al. Optical quantification of intracellular mass density and cell mechanics in 3D mechanical confinement. *Soft Matter* **17**, 853–862 (2021).
139. Mattana, S. et al. Non-contact mechanical and chemical analysis of single living cells by microspectroscopic techniques. *Light Sci. Appl.* **7**, 17139–17139 (2018).
140. Barer, R. Interference microscopy and mass determination. *Nature* **169**, 366–367 (1952).
141. Kim, K. et al. Diffraction optical tomography using a quantitative phase imaging unit. *Opt. Lett.* **39**, 6935–6938 (2014).
142. Montrose, C. J., Solovyev, V. A. & Litovitz, T. A. Brillouin scattering and relaxation in liquids. *J Acoust. Soc. Am.* **43**, 117–130 (2005).
143. Antonacci, G. et al. Spectral broadening in Brillouin imaging. *Appl. Phys. Lett.* **103**, 221105 (2013).
144. Mattarelli, M. et al. Disentanglement of multiple scattering contribution in Brillouin microscopy. *ACS Photonics* **9**, 2087–2091 (2022).
145. Lasch, P. Spectral pre-processing for biomedical vibrational spectroscopy and microspectroscopic imaging. *Chemom. Intell. Lab. Syst.* **117**, 100–114 (2012).
146. Xiang, Y. et al. Multivariate analysis of Brillouin imaging data by supervised and unsupervised learning. *J. Biophotonics* **14**, e202000508 (2021).
147. Xiang, Y., Foreman, M. R. & Torok, P. SNR enhancement in Brillouin microspectroscopy using spectrum reconstruction. *Biomed. Opt. Express* **11**, 1020–1031 (2020).
148. Li, J. et al. Sensitive impulsive stimulated Brillouin spectroscopy by an adaptive noise-suppression matrix pencil. *Opt. Express* **30**, 29598–29610 (2022).
149. Torok, P. & Foreman, M. R. Precision and informational limits in inelastic optical spectroscopy. *Sci. Rep.* **9**, 6140 (2019).
150. Antonacci, G. et al. Quantification of plaque stiffness by Brillouin microscopy in experimental thin cap fibroatheroma. *J. R. Soc. Interface* **12**, 20150843 (2015).
151. Elsayad, K. Spectral phasor analysis for Brillouin microspectroscopy. *Front. Phys.* **7**, 62 (2019).
152. Fioretto, D., Caponi, S. & Palombo, F. Brillouin–Raman mapping of natural fibers with spectral moment analysis. *Biomed. Opt. Express* **10**, 1469–1474 (2019).
153. Jun, L. et al. Minimum volume simplex analysis: a fast algorithm for linear hyperspectral unmixing. *IEEE Trans. Geosci. Remote Sensing* **53**, 5067–5082 (2015).
154. Palombo, F. et al. Hyperspectral analysis applied to micro-Brillouin maps of amyloid-β plaques in Alzheimer's disease brains. *Analyst* **143**, 6095–6102 (2018).
155. Bradbury, P. et al. Timothy grass pollen induces spatial reorganisation of F-actin and loss of junctional integrity in respiratory cells. *Inflammation* **45**, 1209–1223 (2022).
156. Krafft, C. et al. Disease recognition by infrared and Raman spectroscopy. *J. Biophotonics* **2**, 13–28 (2009).
157. Bao, G. & Suresh, S. Cell and molecular mechanics of biological materials. *Nat. Mater.* **2**, 715–725 (2003).
158. Discher, D. E., Janmey, P. & Wang, Y. L. Tissue cells feel and respond to the stiffness of their substrate. *Science* **310**, 1139–1143 (2005).
159. Janmey, P. A. & McCulloch, C. A. Cell mechanics: integrating cell responses to mechanical stimuli. *Annu. Rev. Biomed. Eng.* **9**, 1–34 (2007).
160. Bershadsky, A., Kozlov, M. & Geiger, B. Adhesion-mediated mechanosensitivity: a time to experiment, and a time to theorize. *Curr. Opin. Cell Biol.* **18**, 472–481 (2006).
161. Hu, S. H. et al. Intracellular stress tomography reveals stress focusing and structural anisotropy in cytoskeleton of living cells. *Am. J. Physiol. Cell Physiol.* **285**, C1082–C1090 (2003).
162. Ingber, D. E. Cellular mechanotransduction: putting all the pieces together again. *FASEB J.* **20**, 811–827 (2006).
163. Antonacci, G. & Braakman, S. Biomechanics of subcellular structures by non-invasive Brillouin microscopy. *Sci. Rep.* **6**, 37217 (2016).
164. Coppola, S. et al. Quantifying cellular forces and biomechanical properties by correlative micropillar traction force and Brillouin microscopy. *Biomed. Opt. Express* **10**, 2202–2212 (2019).
165. Elsayad, K. et al. Mapping the subcellular mechanical properties of live cells in tissues with fluorescence emission–Brillouin imaging. *Sci. Signal.* **9**, rs5 (2016).
166. Zhang, J. et al. Brillouin flow cytometry for label-free mechanical phenotyping of the nucleus. *Lab Chip* **17**, 663–670 (2017).
167. Abuhattum, S. et al. Adipose cells and tissues soften with lipid accumulation while in diabetes adipose tissue stiffens. *Sci. Rep.* **12**, 10325 (2022).
168. Krachmer, J. H., Feder, R. S. & Belin, M. W. Keratoconus and related noninflammatory corneal thinning disorders. *Surv. Ophthalmol.* **28**, 293–322 (1984).
169. Jun, A. S. et al. Subnormal cytokine profile in the tear fluid of keratoconus patients. *PLoS ONE* **6**, e16437 (2011).
170. Rabinowitz, Y. Ectasia after laser in situ keratomileusis. *Curr. Opin. Ophthalmol.* **17**, 421–427 (2006).
171. Binder, P. S. et al. Keratoconus and corneal ectasia after LASIK. *J. Refract. Surg.* **21**, 749–752 (2005).
172. Roy, A. S. & Dupps, W. J. Jr Patient-specific computational modeling of keratoconus progression and differential responses to collagen cross-linking. *Invest. Ophthalmol. Vis. Sci.* **52**, 9174–9187 (2012).
173. Meek, K. et al. Changes in collagen orientation and distribution in keratoconus corneas. *Invest. ophthalmol. Vis. Sci.* **46**, 1948–2004 (2005).
174. Morishige, N. et al. Second-harmonic imaging microscopy of normal human and keratoconus cornea. *Invest. Ophthalmol. Vis. Sci.* **48**, 1087–1181 (2007).
175. Zimmermann, D. R. et al. Comparative studies of collagens in normal and keratoconus corneas. *Exp. Eye Res.* **46**, 431–442 (1988).
176. Petsche, S. J. & Pinsky, P. M. The role of 3-D collagen organization in stromal elasticity: a model based on X-ray diffraction data and second harmonic-generated images. *Biomech. Model. Mechanobiol.* **12**, 1101–1113 (2014).
177. Zhang, H. et al. Motion-tracking Brillouin microscopy for in-vivo corneal biomechanics mapping. *Biomed. Opt. Express* **13**, 6196–6210 (2022).
178. Ambekar, Y. et al. Multimodal quantitative optical elastography of the crystalline lens with optical coherence elastography and Brillouin microscopy. *Biomed. Opt. Express* **11**, 2041–2051 (2020).
179. Besner, S. et al. In vivo Brillouin analysis of the aging crystalline lens. *Invest. Ophthalmol. Vis. Sci.* **57**, 5093–5100 (2016).
180. Liu, W. & Wang, Z. Current understanding of the biomechanics of ventricular tissues in heart failure. *Bioengineering* **7**, 2 (2020).
181. Villalba-Orero, M. et al. Assessment of myocardial viscoelasticity with Brillouin spectroscopy in myocardial infarction and aortic stenosis models. *Sci. Rep.* **11**, 21369 (2021).
182. Libby, P. Mechanisms of acute coronary syndromes. *N. Engl. J. Med.* **369**, 883–884 (2013).
183. VIRMANI, R. et al. Pathology of the thin-cap fibroatheroma. *J. Interv. Cardiol.* **16**, 267–272 (2003).
184. Mathieu, V. et al. Micro-Brillouin scattering measurements in mature and newly formed bone tissue surrounding an implant. *J. Biomech. Eng.* **133**, 021006 (2011).
185. Matsukawa, M. et al. Application of a micro-Brillouin scattering technique to characterize bone in the GHz range. *Ultrasonics* **54**, 1155–1161 (2014).
186. Akilbekova, D. et al. Brillouin spectroscopy and radiography for assessment of viscoelastic and regenerative properties of mammalian bones. *J. Biomed. Opt.* **23**, 097004 (2018).
187. Wu, P.-J. et al. Detection of proteoglycan loss from articular cartilage using Brillouin microscopy, with applications to osteoarthritis. *Biomed. Opt. Express* **10**, 2457–2466 (2019).
188. Guck, J. et al. Optical deformability as an inherent cell marker for testing malignant transformation and metastatic competence. *Biophys. J.* **88**, 3689–3698 (2005).
189. Cross, S. E. et al. Nanomechanical analysis of cells from cancer patients. *Nat. Nanotechnol.* **2**, 780–783 (2007).
190. Soteriou, D. et al. Rapid single-cell physical phenotyping of mechanically dissociated tissue biopsies. *Nat. Biomed. Eng.* **7**, 1392–1403 (2023).
191. Plodinec, M. et al. The nanomechanical signature of breast cancer. *Nat. Nanotechnol.* **7**, 757–765 (2012).
192. Kumar, S. & Weaver, V. M. Mechanics, malignancy, and metastasis: the force journey of a tumor cell. *Cancer Metastasis Rev.* **28**, 113–127 (2009).
193. Gensbittel, V. et al. Mechanical adaptability of tumor cells in metastasis. *Dev. Cell* **56**, 164–179 (2021).
194. Roberts, A. B. et al. Tumor cell nuclei soften during transendothelial migration. *J. Biomech.* **121**, 110400 (2021).
195. Cao, X. et al. A chemomechanical model for nuclear morphology and stresses during cell transendothelial migration. *Biophys. J.* **111**, 1541–1552 (2016).
196. Conrad, C. et al. Mechanical modulation of tumor nodules under flow. *IEEE Trans. Biomed. Eng.* **69**, 294–301 (2021).
197. Wisniewski, E. et al. Dorsoventral polarity directs cell responses to migration track geometries. *Sci. Adv.* **6**, eaba6505 (2020).
198. Koehl, M. A. R. Biomechanical approaches to morphogenesis. *Seminars in Developmental Biology* **1**, 367–378 (1990).
199. Miller, C. J. & Davidson, L. A. The interplay between cell signalling and mechanics in developmental processes. *Nat. Rev. Genet.* **14**, 733–744 (2013).

200. Heer, N. C. & Martin, A. C. Tension, contraction and tissue morphogenesis. *Development* **144**, 4249–4260 (2017).
201. Handler, C., Scarcelli, G. & Zhang, J. Time-lapse mechanical imaging of neural tube closure in live embryo using Brillouin microscopy. *Sci. Rep.* **13**, 263 (2023).
202. Viola, J. M. et al. Tubule jamming in the developing kidney creates cyclical mechanical stresses instructive to in vitro nephron formation. Preprint at *bioRxiv* https://doi.org/10.1101/2022.06.03.494718 (2022).
203. Ambekar, Y. S. et al. Multimodal imaging system combining optical coherence tomography and Brillouin microscopy for neural tube imaging. *Opt. Lett.* **47**, 1347–1350 (2022).
204. Sun, W. et al. The bioprinting roadmap. *Biofabrication* **12**, 022002 (2020).
205. Vedadghavami, A. et al. Manufacturing of hydrogel biomaterials with controlled mechanical properties for tissue engineering applications. *Acta Biomaterialia* **62**, 42–63 (2017).
206. Xiang, Y. et al. Background-free fibre optic Brillouin probe for remote mapping of micromechanics. *Biomed. Opt. Express* **11**, 6687–6698 (2020).
207. Antonacci, G., Elsayad, K. & Polli, D. On-Chip notch filter on a silicon nitride ring resonator for Brillouin spectroscopy. *ACS Photonics* **9**, 772–777 (2022).
208. Randleman, J. B. et al. Subclinical keratoconus detection and characterization using motion tracking Brillouin microscopy. *Ophthalmology* https://doi.org/10.1016/j.ophtha.2023.10.011 (2023).
209. Wu, P.-H. et al. A comparison of methods to assess cell mechanical properties. *Nat. Methods* **15**, 491–498 (2018).
210. Patel, A. et al. A liquid-to-solid phase transition of the ALS protein FUS accelerated by disease mutation. *Cell* **162**, 1066–1077 (2015).

Acknowledgements

The authors thank R. Schlüßler, S. Möllmert, K. Kim, T. Beck, J. Czarske, K. Elsayad, R. Prevedel, G. Antonacci, P. Török, F. Palombo, M. Mattarelli and T. Dehoux for many stimulating discussions. I.K. is supported by the Australian Research Council Centre of Excellence in Optical Microcombs for Breakthrough Science (CE230100006) and the Australian Research Council Centre of Excellence in Quantum Biotechnology (CE230100021). J.Z. is supported by the Eunice Kennedy Shriver National Institute of Child Health and Human Development, National Institutes of Health (NIH) (K25HD097288, R21HD112663). G.S is supported by the National Science Foundation (DBI-1942003) and NIH (R21CA258008, R01EY028666, R01EY030063). A.B. acknowledges the support of the Israel Science Foundation (grant no. 2576/21). S.C. is supported by European Union — NextGenerationEU under the Italian Ministry of University and Research (MUR) National Innovation Ecosystem grant ECS00000041 — VITALITY — CUP B43C22000470005 and PRIN 2022 PNRR P2022RH4HH.

Author contributions

Introduction (I.K. and S.C.); Experimentation (all authors); Results (all authors); Applications (I.K., J.Z., J.G. and G.S.); Reproducibility and data deposition (J.Z., S.C. and I.K.); Limitations and optimizations (J.G., G.S. and S.C.); Outlook (J.G.); Overview of the Primer (all authors).

Competing interests

The authors declare no competing interests.

Additional information

Supplementary information The online version contains supplementary material available at https://doi.org/10.1038/s43586-023-00286-z.

Peer review information *Nature Reviews Methods Primers* thanks Giuseppe Antonacci, Robert Prevedel, Seok Hyun Yun and Vladislav V. Yakovlev for their contribution to the peer review of this work.

Publisher's note Springer Nature remains neutral with regard to jurisdictional claims in published maps and institutional affiliations.

Springer Nature or its licensor (e.g. a society or other partner) holds exclusive rights to this article under a publishing agreement with the author(s) or other rightsholder(s); author self-archiving of the accepted manuscript version of this article is solely governed by the terms of such publishing agreement and applicable law.

Related links

Bio-Brillouin Society: https://www.biobrillouin.org/

© Springer Nature Limited 2024